2014-01-05

Collisional Dynamic Elements of the Pyrazine - N2O System:Middle and Low J States

La Moyne Tyler Mix
Brigham Young University - Provo

Collisional Dynamic Elements of the Pyrazine – N_2O System:

Middle and Low J States

LaMoyne Tyler Mix

A thesis submitted to the faculty of
Brigham Young University
in partial fulfillment of the requirements for the degree of

Master of Science

Eric T. Sevy, Chair
Steven R. Goates
Matthew C. Asplund

Department of Chemistry and Biochemistry

Brigham Young University

January 2014

ABSTRACT

Collisional Dynamic Elements of the Pyrazine – N_2O System:
Middle and Low J States

LaMoyne Tyler Mix
Deparment of Chemistry and Biochemistry, BYU
Master of Science

Unimolecular reactions based on the Lindemann – Hinchelwood mechanism are important to understanding combustion and atmospheric processes. The main feature of this mechanism is the energy transfer probability distribution function, P(E´,E). We have chosen to study P(E´,E) through gas phase collisional dynamics probed with IR transient absorption spectroscopy. Post-collision absorption line widths for the pyrazine-N_2O system are used to calculate lab frame translational temperatures. The translational temperatures reveal that collisions with large rotational energy transfer also transfer large amounts of translational energy. For J states >47 the relationship is linear indicating a constant impact parameter. Line widths for J=47 through J=59 also showed that there is no out-scattering from these states, in contrast to work performed previously in the Sevy group. The discrepancy between these measurements prompted a complete analysis of the causes of noise in the experimental system. Defective instruments were identified and noise sources localized, including IR diode frequency jitter. Improved experimental techniques and troubleshooting guides are explained for future researchers in the Sevy group.

Keywords: Collisional Dynamics, Energy Transfer, IR Transient Absorbtion, Eric T. Sevy, LaMoyne Tyler Mix

Table of Contents

List of Tables

List of Figures

Chapter 1:

Introduction to IR Transient Absorption Spectroscopy

Chapter 1: Introduction to IR Transient Absorption Spectroscopy

Gas phase reaction mechanisms are inherently complex because they involve many types of elementary reactions, including unimolecular isomerizations, eliminations, dissociations, and recombinations. For example, there are forty elementary reactions in methanol combustion[1], two thirds of which are unimolecular processes. A complete kinetic analysis of methanol combustion would require successful determination of the rate constants for all forty reactions. Measuring the rates experimentally is time consuming and difficult if not impossible because all of the elementary reactions cannot be isolated. To facilitate *a priori* calculations of the unimolecular rate constants, Frederick Lindemann[2] proposed breaking up the reaction process into three steps. The first step involves collisional energy transfer between the molecule of interest or donor, designated A, and a second molecule of the surrounding gas, B, known as the bath(1). This step produces an excited molecule A* with sufficient energy to overcome the reaction activation barrier. The excited donor molecule, A*, can either be deactivated by a second collision with a molecule of bath gas (2), or react to form products, P(3).

$$A + B \xleftrightarrow{k_1} A^* + B \qquad (1)$$

$$A^* + B \xleftrightarrow{k_2} A + B \qquad (2)$$

$$A^* \xrightarrow{k_{uni}} P \qquad (3)$$

The collisional energy transfer steps (1 & 2) can be assumed to be much faster that the reaction step (3) at low temperatures and/or high pressures. Therefore the steady state approximation can be invoked for A* and the overall rate constant is[3]:

$$\frac{d[P]}{dt} = k_{uni}[A^*] = \frac{k_1 k_2 [A][B]}{k_{uni} + k_2[B]} \quad (4)$$

Because it limits the donor to only two states, A and A*, the Lindemann description is qualitatively correct but does not provide accurate quantitative rate constants. The model assumes that every collision is either activating or deactivating. In other words every collision transfers the same magnitude of energy:

$$\Delta E = E(A^*) - E(A) \quad (5)$$

In real systems there are large numbers of states and collisional energy transfer occurs between all possible combinations of states with varying magnitudes of ΔE. Cyril Hinshelwood[4] recognized the correct formulation of unimolecular rate constants would include microscopic collision rates between every state and energy dependent reaction rates. Figure 1.1 illustrates the expansion of the Lindemann model to multiple states. To account for all the possible collision and reaction rates, Hinshelwood introduced the energy transfer probability distribution function, P(E′,E) and energy dependent rate constants, k(E). P(E′,E) describes the likelihood of the donor changing from a state E to state E′ as a result of a single collision. Rate constants k(E) are nonzero if E is greater than E^*, the minimum energy required for reaction.

The total rate constant, k_{uni}, is calculated by combining P(E,E′) for activating collisions, P(E′,E) for deactivating collisions, and k(E). Because the state densities around E^* for most unimolecular reactions are very high, at least 10^{15} states per wavenumber, (cm^{-1}), integration is preferred over summation.

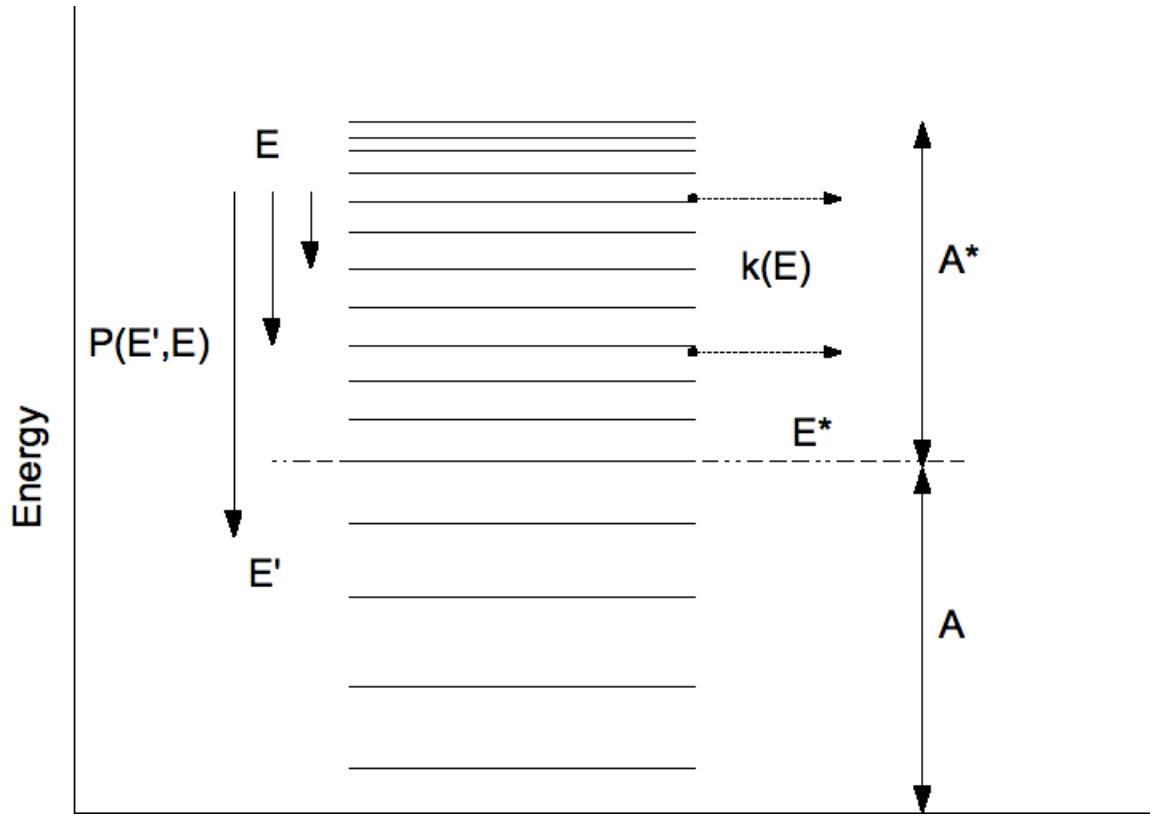

Figure 1.1 Examples of possible deactivating energy transfer events between states and reaction events in the expanded Lindemann-Hinshelwood model. The horizontal lines represent energy levels of the donor molecule, which increase from bottom to top. E* is the minimum energy required to react as in equation (3). The downward arrows on the left represent deactivating collisions with the donor beginning at energy E above the barrier and finishing at some energy E′. The function P(E′,E) is the probability of that collisional energy transfer event occurring. The horizontal arrows on the right represent the reaction of donor molecules at a rate of k(E). In the basic Lindemann model all these states were grouped together into A* and A. Hinshelwood modified the model by including all the energy states. This allows for collisional energy transfer to occur completely above the E* barrier as well as across the barrier.

The master equation for computing the macroscopic rate constant, k_{uni}, from the molecular functions is[5]:

$$-k_{uni}g(E) = \omega \int_0^{\infty} [\,\mathrm{P}(E,E')\mathrm{g}(E') - \mathrm{P}(E',\mathrm{E})\mathrm{g}(E)]\, dE - k(E)g(E) \qquad (6)$$

where *g(E)* is the population of reactant molecules with energy E, and ω is the collision frequency. This equation can be solved reliably using numerical methods in seconds on a personal computer provided the constitute functions are known. The populations, *g(E)* can be calculated from Boltzmann statistical mechanics, the collision frequency, ω, can be approximated from the Lennard-Jones impact potentials and the rate constants, $k(E)$, can be estimated from RRKM theory[5]. Developing a general model for P(E′,E) from simple physical properties of the donor and bath is the key to accurate *a priori* calculations of unimolecular rate constants.

There are several methods to experimentally determine P(E′,E). In all methods a highly excited donor molecule, typically ~40,000 cm^{-1}, is produced. Methods differ in the way that they detect the collisional energy transfer. Infrared fluorescence[6,7] (IRF) and ultraviolet absorbtion[8] (UVA) measure average energy transfer per collision, $\langle \Delta E \rangle$, of the donor molecule. IRF and UVA studies assume a functional form for P(E′,E) and find the proper fit with the observed $\langle \Delta E \rangle$ to this function type. IRF and UVA studies are indirect calculations of P(E′,E). Luther and coworkers[9,10] developed Kinetically Controlled Selective Ionization (KCSI) to measure donor populations at specific energies following multiple collisions and extract P(E′,E) in its correct functional form. KCSI studies are not state specific and average the effects of collisional energy transfers for many collisions. We have approached finding P(E′,E) by infrared diode transient spectroscopy as pioneered by Flynn and Weston[11]. This technique augments IRF, UVA, and KCSI because it allows

measurement of P(E′,E) in its correct functional form and dynamic information on the collisional potential energy surface.

At the core of IR diode transient spectroscopy is the law of conservation of energy. In a deactivating collision, equation (2), the energy lost by the donor molecule is the same as the energy gained by the bath molecule. Because the bath molecules are often simple diatomic or triatomic species, the bath energy gain can be measured more accurately than the donor energy loss. Using IR absorption, we directly observe individual vibrational and rotational state populations and translational energy distributions of the simpler bath molecules. Flynn and coworkers[12] showed that the state resolved energy distributions can be used to construct energy transfer rate constants and exact P(E′,E) distributions. Knowing the distribution of collisional energy among the degrees of freedom of the bath molecules contributes to understanding the collisional potential energy surface. IR diode transient absorption also allows us to change each collisional partner independently and without major expense.

Intelligent selection of the collision pairs isolates specific physical properties of the donor and bath molecules for study. Michaels et al.[13] determined that vibrational energy transfer, V – V, between pyrazine and CO_2 is dominated by long-range attractive electrostatic forces. They predicted, and Mullin and coworkers[14] confirmed, that aromatic donors with dipole moments should have larger V – V energy transfer probabilities. In contrast, rotational and translational energy transfer, V – RT, is dominated by short-range implusive interactions between the collision pair[11]. Sevy et al.[15] showed by comparisons of pyrazine and 2-methylpyrazine that low frequency donor vibrational modes contribute the most to P(E′,E) with CO_2 bath. The low frequency out-of-plane bending modes contribute

significantly more and are referenced to gateway modes. In addition, Sevy et al[15] showed that the vibrational state densities of aromatic donor molecules is a close representation of the functional shape of P(E′,E). Further studies with pyridine,[16] pyrimidine,[17] and the diflouro-benznes[18] as donors confirmed that molecules with more low frequency gateway modes have larger V - RT probabilities. A large body of work has been performed with aromatic donors and CO_2 bath leaving many other collisional pairs unexplored. Recent work has been focused on how bath properties influence P(E′,E) by comparing H_2O[19], CO_2[15] and N_2O[20]. Similar to the donor studies, bath dipole moments are implicated in V –V processes while the moment of inertia may be an important characteristic of V – RT processes.

However, all of these studies share a common limitation: only large ΔE (>2000 cm^{-1}) collisions were measured in the calculation of P(E′,E) while the probability of smaller ΔE events were found by extrapolation. This is a result of measuring transient absorbances for only high (~60-80) J states of the bath molecules. High J states are much easier to collect absorbances experimentally and analyze the results than low and mid J state measurements. The preference for high J states is a result of two connected reasons: they have essentially zero precollsion population and they are far from the average state in the room temperature rotational distribution. These conditions lead to collisional scattering solely into the selected J state, and small ΔE errors in approximating the initial state as the average state.

The mid and low J states are more difficult to measure and analyze because there is a precollision population. Upon probing a specific state these bath molecules may be scattered out of the probe state to some other state, they may be scattered from a different

state into the probe state, or they may not collide at all in the time scale of the study. Absorption siganls from molecules that don't collide are removed by only looking at the change in IR absorption. We believe that we can identify and correct for both out scattering from and in scattering to specific J states by appropriate data analysis and curve fitting. We can then compare P(E′,E) measured from mid and low J states to P(E′,E) measured from high J states.

The focus of this work is to measure V – RT energy transfer for the low (~0-40) and mid(~40-60) J states of the pyrazine-N_2O system, evaluate the validity of the extrapolation of P(E′,E) to small ΔE from the high J states experiment, and uncover the effect of an assumed collisional rate constant on P(E′,E). If the extrapolation method is valid, future studies can continue to extrapolate P(E´,E) from measuring only the high J states for other collisional pairs. Measuring only the high J states would decrease the difficulty and decrease the time required to obtain P(E´,E) allowing more collisional pairs to be studied at a faster pace.

References

1. Dove, J.E. and Warnatz, J. (1983), *Ber. Bunsenges. Phys. Chem.*, **87**, 1040
2. Lindemann, F.A. (1922), *Trans. Faraday Soc.,* **17,** 598.
3. Atkins, P., de Paula, J., Friedman, R., (2009), *Quanta, Matter, and Change;* W.H. Freeman and Company: New York, New York. (640)
4. Hinshelwood, C.N. (1926), *Proc. Roy. Soc. (London),* **A113,** 230.
5. Gilbert, R.G., Smith, S.C., (1990) *Theory of Unimolecular and Recombination Reactions;* Blackwell Scientific Publications: Oxford, England. (213)
6. Miller, L.A. and Barker, J.R., (1996), *J. Chem. Phys.,* **105,** 1383
7. Miller, L.A., Cooks, C.D., and Barker. J.R., (1996), *J. Chem. Phys.,* **105,** 3012
8. Hippler, H., Otto, B., and Troe, J., (1989), *Ber. Bunsenges. Phys. Chem.*, **93**, 428.
9. Hold, U., Lenzer T., Luther, K., Reihs, K., and Symonds, A.C., (2000) *J. Chem. Phys.* **112,** 4076.
10. Lenzer, T., Luther, K., Reihs, K., and Symonds, A.C., (2000) *J. Chem. Phys.* **112,** 4090.
11. Flynn, G.W. and Weston Jr., R.E., (1993) *J. Chem. Phys.* **97,** 8116.
12. Michaels, C.A. and Flynn, G.W., (1997) *J. Chem. Phys.* **106,** 3558.
13. Michaels, C.A., Mullin A.S. and Flynn G.W., (1995) *J. Chem. Phys.* **102,** 6682.
14. Wall, M. C., Stewart, B. A., Mullin, A. S. (1998) *J. Chem. Phys.* **108,** 6185.
15. Sevy, Eric T., Rubin, Seth M., Lin, Zhen, Flynn, George W; (2000) *J. Chem. Phys.* ***113,*** *4912.*
16. Johnson, J. A., Duffin, A. M., Hrn, B. J., Jackson, K. E., Sevy, E. T.; (2008) *J. Chem. Phys.*
17. Johnson J. A., Kim, K., Mayhew, M. Mitchell, D. G., Sevy, E. T.; (2008) *J. Phys. Chem. A*

18. Mitchell, D. G., Johnson, A. M., Johnson J. A., Judd, K. A., Kim, K.. Mayhew, M., Powell, A. L., Sevy, E. T.; (2008) *J Phys. Chem. A.* **112,** 1157.

19. Elioff, M. S., Fraelich, M., Sansom, R. L., Mullin, A. S. (1999) *J Chem. Phys.* ***111,*** 3517.

20. Kim, Kilyoung. Ph. D. Dissertation, Brigham Young University, UT, April 2011.

Chapter 2:

Experimental Setup

Chapter 2: Experimental Setup

The experimental setup is similar to other IR diode transient absorption systems[1,2] and has been fully described by Johnson et al[3]. Chapter 4 of this work contains detailed experimental techniques for performing IR transient absorption measurements. Each piece of equipment was selected to facilitate a three step energy transfer scheme. First, pyrazine is pumped by UV light at 248 nm, finishing in a highly excited vibrational state with energy E (1). Collisions transfer energy between the excited pyrazine and the N_2O, scattering the N_2O into excited rotational states of the ground vibrational state (2). Last, the post-collision populations of the N_2O rotational states are probed by IR absorbance at 4.6 μm into the first vibrational state(3).

$$Pyrazine + h\nu\ (248\ nm) \rightarrow Pyrazine^{E}\ (E_{vib} = \sim 41{,}000\ cm^{-1}) \qquad (1)$$

$$Pyrazine^{E} + N_2O \rightarrow Pyrazine^{E'} + N_2O\ (00^{0}0, J) \qquad (2)$$

$$N_2O\ (00^{0}0, J) + h\nu\ (4.6\ \mu m) \rightarrow N_2O\ (00^{0}1, J \pm 1) \qquad (3)$$

Figure 2.1 shows the typical layout of our experimental setup. Green shapes and lines correspond to the sample cell and the low pressure vacuum system. Pyrazine (Sigma-Aldrich 99% pure) is further purified by three freeze (77K)-pump-thaw (298 K) cycles before use. 10 mTorr N_2O (Intermountain Airgas, 99.9999% pure) is mixed with 10 mTorr of pyrazine via solonoid valves (MKS Type 248) monitored by capacitance monometers (MKS Type 626A and 627A). Using a 1:1 mixture of the two gasses increases the probability of collisions occurring between the excited pyrazine and N_2O. The total pressure of 20 mTorr was selected to decrease the mean collision time to 4μs. The gas then flows into an IR sample cell with CaF_2 windows. Sample cells of 20, 100, 200 and 300

cm in length can be exchanged to adjust the absorption path length. The flow rate of the diffusion pump backed by a rotary vane mechanical pump (Alcatel) is sufficient to replace the gas in the cell every second. The reference cell is filled with N_2O at a static pressure of ~200 mTorr. The gas flow cell and the reference cell remain at constant pressure throughout each experimental session.

The 248 nm UV light used to excite the pyrazine, corresponding to blue items in Figure 2.1, is supplied by a KrF excimer laser (Lamda Physik Compex 201). Pyrazine undergoes an initial electronic transition, $S_2 \leftarrow S_o$ followed by rapid radiationless internal conversion to a high vibrational excited state in the ground electronic state (Eq. 1). We regulate the laser power to between 4-6 mJ/cm^2 using a Brewster stack to ensure single photon absorption. The excimer repetition rate is controlled by a digital delay generator (Stanford Research Sys. Model DG645) triggered off the modulation cycle of the IR diode. Firing at 1 Hz each pulse will energize new, previously unexcited, gas as it flows through the sample cell.

The IR light, shown in red in Figure 2.1, is propagated collinearly with the UV beam through the sample cell. It is produced by a continuous wave lead salt diode laser (Laser Components L5736 Rig and L5830 Controller) tunable from 2165 – 2215 cm^{-1} with a frequency bandwidth of 0.0003 cm^{-1}. After passing through the sample cell, the IR light is passed into a single grating monochromator (Acton Research Corp. SpectraPro 500i) to select a single laser mode. Finally, the light is detected by a LN_2 cooled InSb photovoltaic diode detector (Judson Tech.) coupled to a pre-amplifier (Perry Amplifiers).

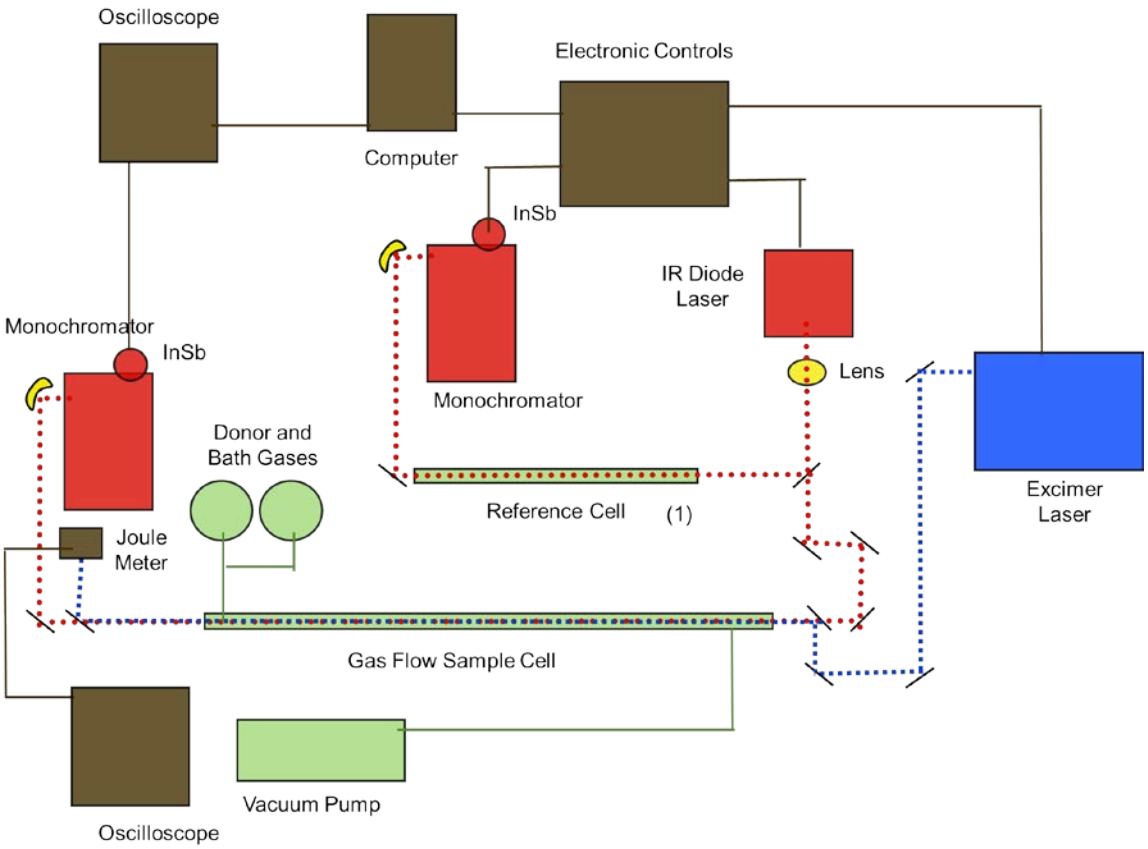

Figure 2.1 Block diagram of experimental setup for infrared diode transient absorption spectroscopy. Green corresponds to vacuum systems, blue to UV laser and UV beam path, red to IR laser and IR beam path, yellow to optics, and brown to electronics. The shown configuration with the reference cell is for measuring line centers. To measure line widths, the reference cell *(1)* is removed and replaced by a scanning Fabry-Perot etalon.

The rise time of the detector and amplifier combination is ~400 ns, 10 times faster than the mean collision time of 4 μs at 20 mTorr. A digital oscilloscope (LeCroy LT364, 500MHz) records the detector output from 2μs before to 18 μs after the excimer laser pulse. A ratio of the AC-coupled signal over the DC-coupled signal is proportional to IR absorbance[4] and is known as the transient.

Before the IR laser beam reaches the sample, ~4% of the light is split off by a CaF_2 window and directed to a reference line. This beam line has either the static reference cell or a scanning Fabry-Perot confocal etalon (Laser Components L5945) installed depending on the experiment type. The light from the reference cell or etalon is then directed into another monochromator (Acton Research Corp. SpectraPro 300i) and focused on to a second pre-amplifier (Perry Amplifiers) coupled InSb detector (Jusdson Tech.). Because the reference line only has 4% of the total IR power, the signal is amplified a second time (Tektronix AM 502) before going to a lock-in amplifier (Stanford Research Sys. SR510). The lock-in amplifier corrects for long-term drifts in the IR diode frequency while measuring the transients, or to scan the frequency during line width measurments.

A Linux based computer is the master controller for the electronics in the experiment, shown in brown in Figure 2.1. The computer runs several Labview programs (National Instruments v8.5) that send trigger pulses to the excimer laser, adjust the etalon, and collect the transients from the digital oscilloscope. Final data analysis of the transients is performed using Matlab (ver. 2013).

This setup is used to record two types of measurements: line centers and line widths. Line centers are collected with the static N_2O cell in the reference line. This allows the IR diode frequency to lock to the exact center of the desired rotational transition. The transient

signal is averaged over ~100 UV laser shots to obtain the peak absorbance value. Line widths are collected with the Fabry-Perot etalon installed in the reference line. The IR diode frequency is locked to an etalon fringe. By scanning the etalon we can alter the IR diode frequency by very small (10^{-4} cm^{-1}) known increments, as illustrated by Figure 2.2. Transients are averaged for 25 shots at 50 frequencies across an individual rotational transition giving the exact line shape and width of the post-collision population. For each line width experiment the etalon is scanned across the transition 4 times. The Doppler-broadened full width at half maximum, referred to by FWHM, is obtained by fitting each pass of the line shapes individually to Gaussian curves. The FWHM combined with the peak absorbance allows us to calculate the post-collision populations, other second level properties, and P(E',E).

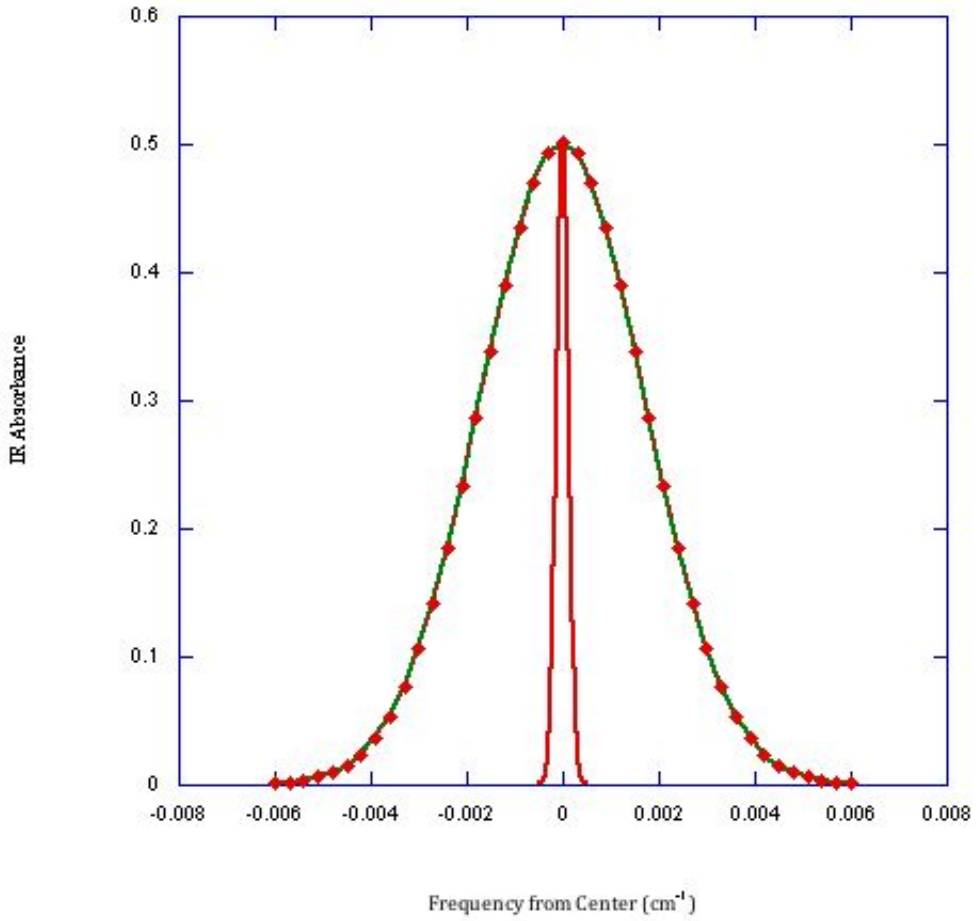

Figure 2.2 To find post-collision line widths the IR diode is locked to a fringe of the scanning Fabry-Perot etalon. Because the diode bandwidth is an order of magnitude smaller than a room temperature N_2O line, we can scan the diode across the line, shown by the red arrows, using the etalon. Transients are collected and averaged for 25 shots at each position, represented by the red squares, to map out the line shape.

References

1. Flynn, G.W. and Weston Jr., R.E., (1993) *J. Chem. Phys.* **97,** 8116.
2. Sevy, Eric T., Rubin, Seth M., Lin, Zhen, Flynn, George W; (2000) *J. Chem. Phys.* ***113,*** *4912.*
3. J. A. Johnson, A. M. Duffin, B. J. Hom, K. E. Jackson and E. T. Sevy, J. Chem. Phys. **128**, 054304 (2008).
4. A. S. Mullin, C. A. Michaels and G. W. Flynn, J. Chem. Phys. 102, 6032 (1995).

Chapter 3:

The Middle J States of the Pyrazine – N_2O System

Chapter 3: The Middle J States of the Pyrazine – N_2O System

Collisional energy transfer and P(E´,E) for aromatic donors with CO_2 as the bath molecule has been studied extensively[1,2,3,4]. To develop a general model for P(E´,E) based on physical properties, we must understand how the function changes with different bath and donor molecules. We have chosen to use a well-studied donor, pyrazine, and N_2O as the bath molecule. A comparison of N_2O and CO_2 shows they have the same molecular weight, geometry, and electronic structure. Yet N_2O has a different moment of inertia, and dipole moment. These two properties may be responsible for any changes in P(E´,E) compared to the CO_2 – pyrazine system.

The Sevy group[5] has previously measured P(E´,E) for large ΔE (>2000 cm^{-1}) collisions by IR transient absorption of the high (60-80) and mid (40-60) J states of N_2O. The probability of smaller ΔE was found by extrapolation, rather than direct measurement. This work aims to measure P(E´,E) for the low J states of N_2O to validate the extrapolation procedure. It will also provide a check on the previous study by measuring some of the mid J states to confirm that the experimental setup is functioning properly.

I. Results

The spectral foundation for calculating P(E´,E) are line width profiles and line center absorptions for $N_2O\ (00^00, J) \rightarrow N_2O\ (00^00, J \pm 1)$ transitions. Line widths provide information about the translational energy gained by N_2O in the J^{th} rotational state during collisions with pyrazine. Line center absorptions combined with line widths for the same transitions, quantify the rotational energy gained by N_2O. In either case, the raw data consists of IR absorption transients. An example transient from a line width of the P55 transition is shown in Figure 3.1. Transients show the change in IR absorption from 2 μs

before the UV laser fires to 18 μs after the UV laser fires. The early rise in the absorption signal represents the increase in the population of N_2O in the (00^00, 55) state due to collisions with excited pyrazine. The non-linear profile of the signal between 5 μs and 10 μs represents the competition between the continued filling of J=55 by collisions between N_2O and slightly less energetic pyrazine and the depletion of J=55 by rotational relaxation of N_2O. At long times the decrease in absorption represents collisional relaxation towards the thermal distribution of states. The average collision time at a total pressure of 20 mTorr is 4 μs. Further calculations use the 1 μs absorbance value to quantify the effects of a single collision and minimize the number of observed secondary collisions.

To extract the 1 μs absorbance value from noise in the transient signal we fit the transient to a line with the linear least squares method. The time domain of the fit has a large effect on the linear fit parameters due to noise oscillations, see Chapter 4, Section X. Since the pre-excitation absorption should not change with time, the absorbance value at time zero is assumed to be zero for all transients. Therefore the 1 μs absorbance, notated $A_{1\mu s}$, is calculated from

$$A_{1\mu s} = m \quad * 1\ \mu s + 0 \qquad (1)$$

where *m* is the slope of the transient fit from 0-6μs. The same transient analysis procedure is employed for line widths and line centers.

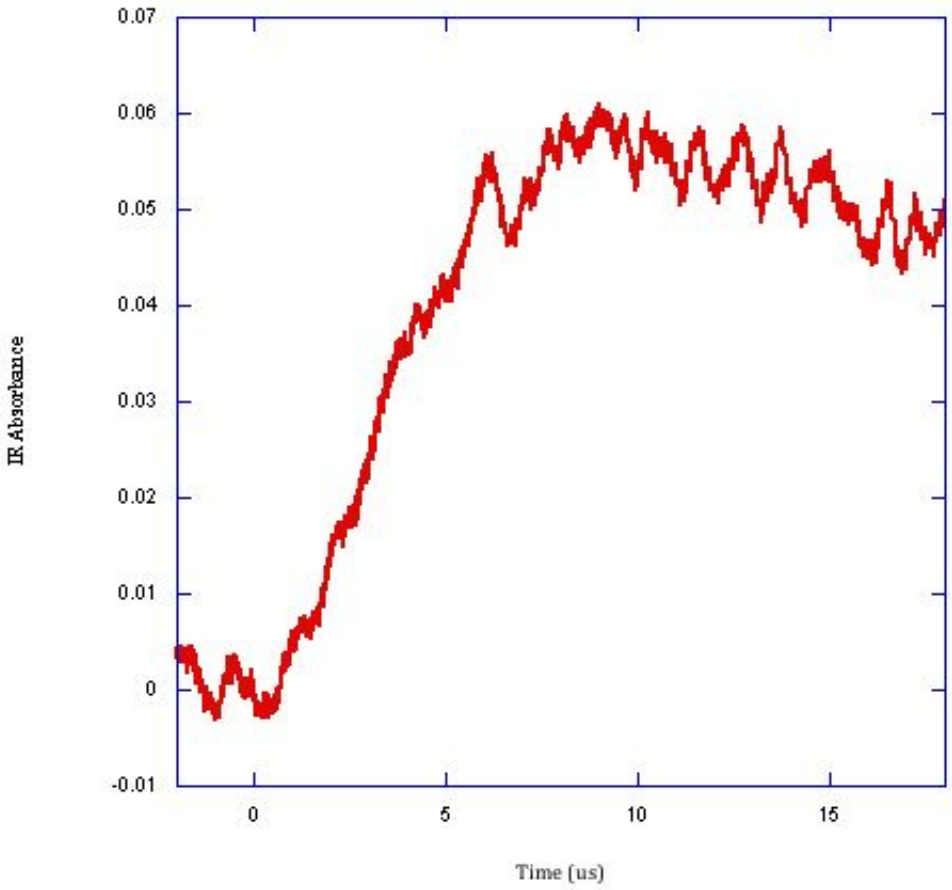

Figure 3.1 A transient absorption signal, averaged over 25 laser shots, shows the change in absorption over time for the transition $N_2O\ (00^00, 55) \rightarrow N_2O\ (00^01, 54)$. The UV laser fires at time zero to excite the pyrazine molecules. The average time for a single collision is 4 μs. The initial linear rise in the signal represents an increase in the population of N_2O in the $(00^00, 55)$ state due to collisions with excited pyrazine.

Line width experiments consist of $A_{1\mu s}$ values recorded at 50 different frequencies centered around the transition of interest. These values are graphed together to form the transient line shape at 1μs. In Figure 3.2, four complete line widths of the p55 transition are depicted. Pass 0, in red, was recorded beginning on the negative frequency side of the peak and scanned to positive frequencies with each new transient measurement. Pass 1, in green, then returned to the starting frequency. The different passes do not entirely overlap in frequency space because of slight hysteresis in the scanning etalon, see Chapter 4, Section VII. Further data analysis treats each pass individually because of this difference.

Ro-vibrational line shapes are determined by the translational character of the molecule's motion due to the Doppler effect. Gaussian shapes are observed when the direction of motion is random and the speed conforms to the Maxwell-Boltzmann distribution. Under our experimental conditions, we are only sensitive to the velocity in the direction of IR light propagation. However, in similar collision experiments the translational motion was shown to be isotropic[1]. Our 1 μs line shapes fit closely to the Gaussian function:

$$A_{fit} = a\left[exp\left(\frac{-4\ln(2)\,(x-b)^2}{\Delta\nu^2}\right)\right] + d \qquad (2)$$

Where the *a* term controls the amplitude of the curve, the *b* term adjusts the position on the x-axis, the *Δν* term is the Full Width at Half of the Maximum amplitude, abbreviated FWHM, and the *d* term adjusts the position on the y-axis. A good Gaussian fit implies that the direction of motion for the N_2O molecules post-collision is random and can be described by a translational temperature. The FWHM parameter from the Gaussian fit of each line, see Eq. (2), is used to calculate a lab frame translational temperature.

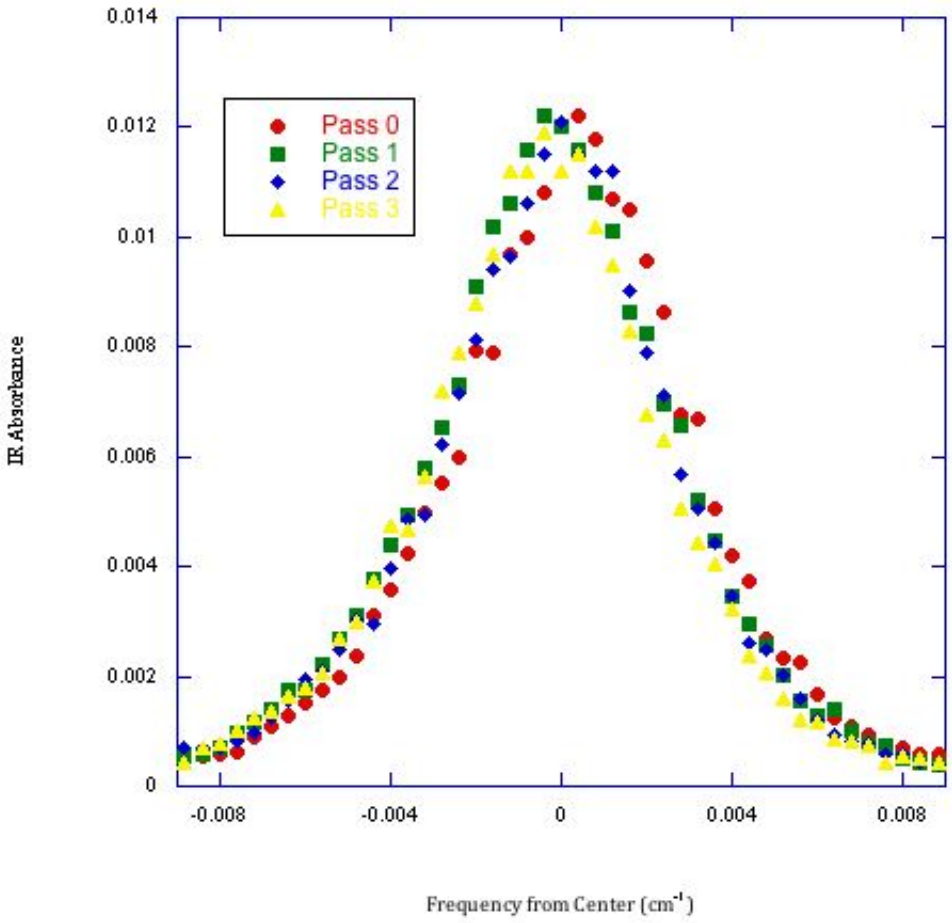

Figure 3.2 Four complete line widths of the P55 transition are shown. Each point represents a 1μs transient absorption signal, see Eq. (1). Pass 0 was measured beginning at low frequency and scanning in the positive direction. Pass 1 returned to the starting point and so forth. The maxima are not all aligned because of a slight hysteresis in the scanning etalon.

$$T_{trans} = \frac{m_{N_2O} c^2 \Delta\nu^2}{8 k_B \ln(2) \nu_0^2} \quad (3)$$

In this equation, m_{N_2O} is the mass of N_2O, c is the speed of light, $\Delta\nu$ is the FWHM, k_B is the Boltzmann constant and ν_0 is the center frequency. Widths and temperatures were then averaged together for multiple passes on different days for the same J state. Table 3.1 lists each of the measured J states with their line widths and translational temperatures. For comparison the average equilibrium line width for the mid J states of N_2O is 0.004 cm^{-1} at 300 K.

Line center measurements were not completed during this work due to external time constraints. Line centers and the calculation of P(E´,E) will be performed in the near future by the Sevy research group.

II. Discussion

For every line width except P41, the 1 μs absorbance FWHM is greater than the thermal equilibrium value 0.004 cm^{-1}. This indicates that collisions between pyrazine and N_2O that scatter molecules into higher J states are accompanied by large translational energy transfers. Energy transfer of rotational and translational energy by collisions is linked. Large translational energy transfers both cause and are the result of large rotational energy transfers.

Plotting the T_{trans} versus J state, see Figure 3.3, highlights two other features of this distribution. First, in the mid J states from P47 to P59 the T_{trans} decreases almost linearly with J states. This correlates with previous experiments on the high J states of the pyrazine-N_2O system[2] and other CO_2 systems[3]. A linear variation means that for these J states the average impact parameter is nearly constant.

Table 3.1 Line Widths and Temperatures Indexed by J State

Peak[a]	Width (cm^{-1})[b]	Temperature (K)[c]
59	0.00740 ± 0.00010	1051 ± 30
58	0.00688 ± 0.00044	910 ± 40
55	0.00686 ± 0.00023	730 ± 55
54	0.00812 ± 0.00068	1257 ± 99
49	0.00491 ± 0.00018	469 ± 34
48	0.00430 ± 0.00010	350 ± 17
47	0.00511 ± 0.00015	495 ± 30
46	0.00511 ± 0.00045	496 ± 85
43	0.00559 ± 0.00038	591 ± 80
41	0.00369 ± 0.00027	258 ± 38

[a] Transitions are from N_2O (00^00, J = X) → N_2O (00^01, J = X-1). This is the P-branch of the anti-symmetric stretch.

[b] Widths are the Full Width at Half Maximum (FWHM) from fitting each pass to a Gaussian function. Widths for the passes on multiple days are averaged together with each value representing 12-16 passes.

[c] Temperatures were calculated individually for each pass from the FWHM according to

$$T_{trans} = \frac{m_{N_2O} c^2 \Delta\nu^2}{8 k_B \ln(2) \nu_0^2}$$

and then averaged together.

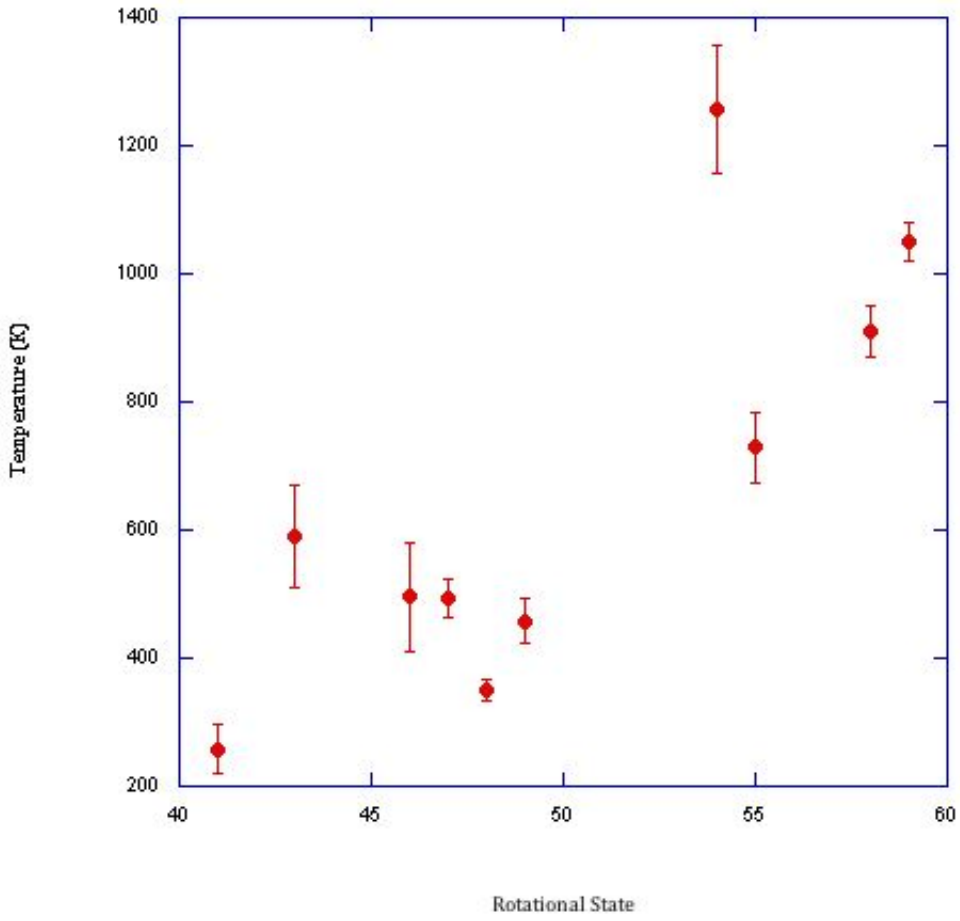

Figure 3.3 T_{trans} vs J state as calculated by Eq (3). The linear decrease in T_{trans} for J=59 to J=47 indicates a constant small impact parameter for collisions transferring both rotational and translational energy to N_2O. From J=47 to J=41, T_{trans} is stable around 450 K. This is a region where glancing collisions with larger impact parameters influence the distribution.

The impact parameter describes the minimum distance between the molecules reached during the collision and is expressed:

$$\frac{h}{2\pi}\Delta J = \mu \Delta v_{rel} b \quad (4)$$

where h is Planck's constant, ΔJ is the change in J state during the collision, μ is the collision reduced mass, Δv_{rel} is the change in relative velocity, and b is the impact parameter. In this experiment ΔJ scales with the final J state, and Δv_{rel} scales with T_{trans}. The linear slope in Figure 3.3 indicates a constant average impact parameter close to 2.5 Å.

Second, below P47 the slope is almost flat with T_{trans} stable around 450 K. Rewriting the impact equation gives:

$$T_{trans} = \frac{2\pi\mu b}{h J_{final}} \quad (5)$$

For T_{trans} to remain constant with the final J state decreasing the impact parameter must be increasing. These are glancing collisions occur at longer ranges between the pyrazine and N_2O.

We expected to see the T_{trans} stablize before 300 K because it is very unlikely that N_2O will donate energy to highly excited pyrazine. P41 does appear to violate this principle by having a narrower line width and a temperature below 300K. Frequency jitter in the diode laser caused the majority of the noise in the P41 line width. Jitter can be corrected by using a shorter sample cell, see Chapter 4, Section XI. Future measurements in the Sevy lab will improve upon the P41 line width.

We have shown that the pyrazine-N_2O is consistent with other transient absorption measurements on systems with CO_2 bath molecules[2,3]. A linear relationship between T_{trans}

and J state exist above J=47, indicating a constant impact parameter. Below J=47 T_{trans} is stable at approximately 450K.

An auxiliary goal when we began measuring the mid J states for N_2O was to provide a check on previous studies already performed by Kim et al[3]. Kim observed double gaussian line shapes in the transient absorptions spectra by from J=56 and below for the pyrazine – N_2O system. Spectra collected in this work from J=59 to J=41 featured only positive single Gaussian line shapes. Determining the correct line shape is critical to a complete understanding of the collision dynamics and P(E´,E).

Line shapes from high J states with low initial populations are dominated by in-scattering with positive amplitudes and Gaussian distributions. Spectra of low J states with high initial populations are predicted to be dominated by out-scattering with negative amplitudes and Gaussian distributions. Spectra from mid J states will have both in-scattering and out-scattering because of a median initial population. Figure 3.4 models the expected behavior for mid J line shapes. The wider positive Gaussian shown in red represents molecules with an increased translational temperature scattering into the states after a collision. The narrower negative Gaussian shown in blue represents molecules beginning at room temperature which are scattered out of the state by a collision. The combination of the two effects is a double Gaussian line shape shown in green.

Figure 3.5 shows two examples of line widths recorded by Kim et al. and in this work. In each plot the vertical axes are independent from each other. The horizontal axes are equivalent in both cases Spectra from Kim et al. are shown in red with the left vertical axis and spectra from this work are in green on the right vertical axis. Both spectra recorded in this work are cleaner with less noise than those collected by Kim et al. The

additional noise in the spectra by Kim et al. may be due to collection with the malfunctioning DDG, see Chapter 4, Section VIII. Upon further examination, the spectra by Kim et. al. were found to be averages of multiple passes on the same day. However, each pass exhibits a large hysteresis effect from the scanning etalon, see Chapet 4, Section VII. Averaging passes with mismatched center frequencies will contribute to the noise and influence the line shape. The combination of the unrecognized fault in the DDG timing and the mistreated hysteresis effect resulted in a false double Gaussian shape.

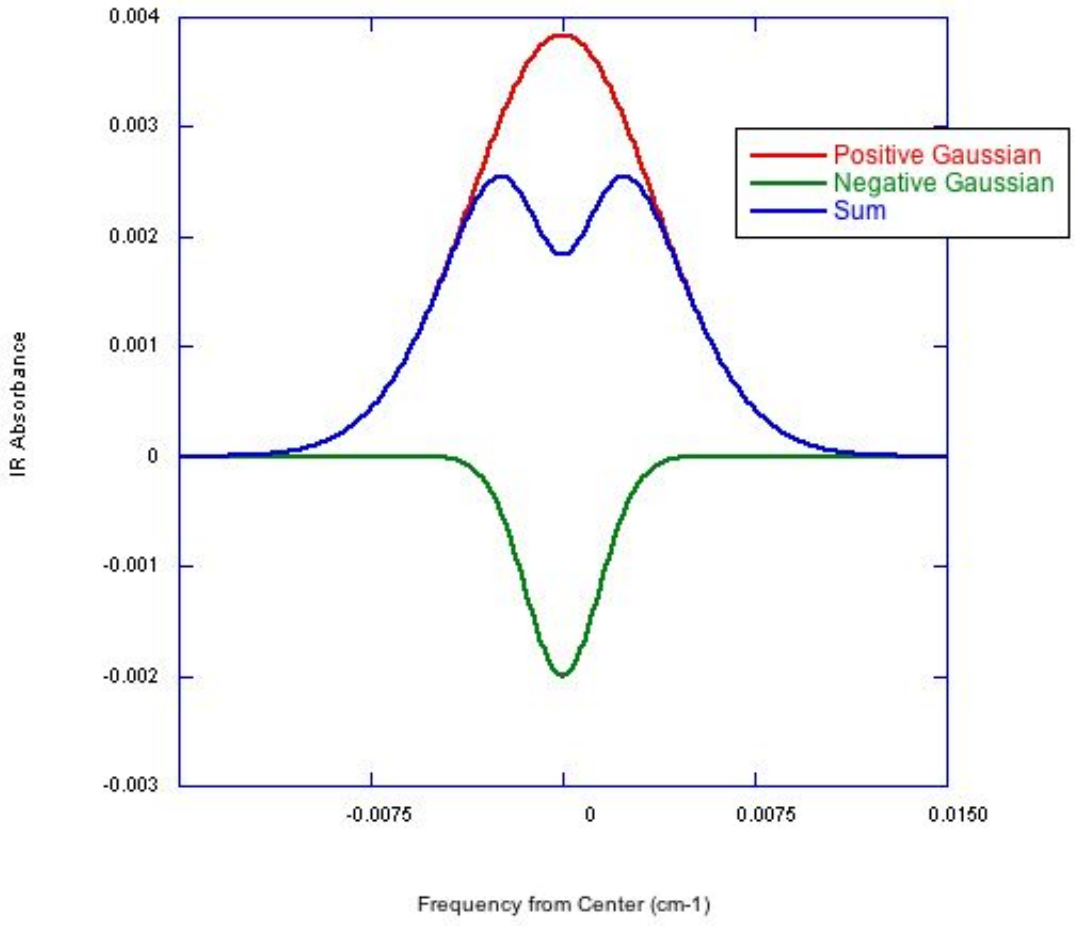

Figure

Figure 3.4 The expected shape for the Mid J line widths. The positive Gaussian in red models absorption by molecules scattered into the probed J state. The negative Gaussian in green models the bleach from molecules that are scattered out of the probed J state by collisions. The expected line shape is the sum of these two absorption events giving a double Gaussian shape.

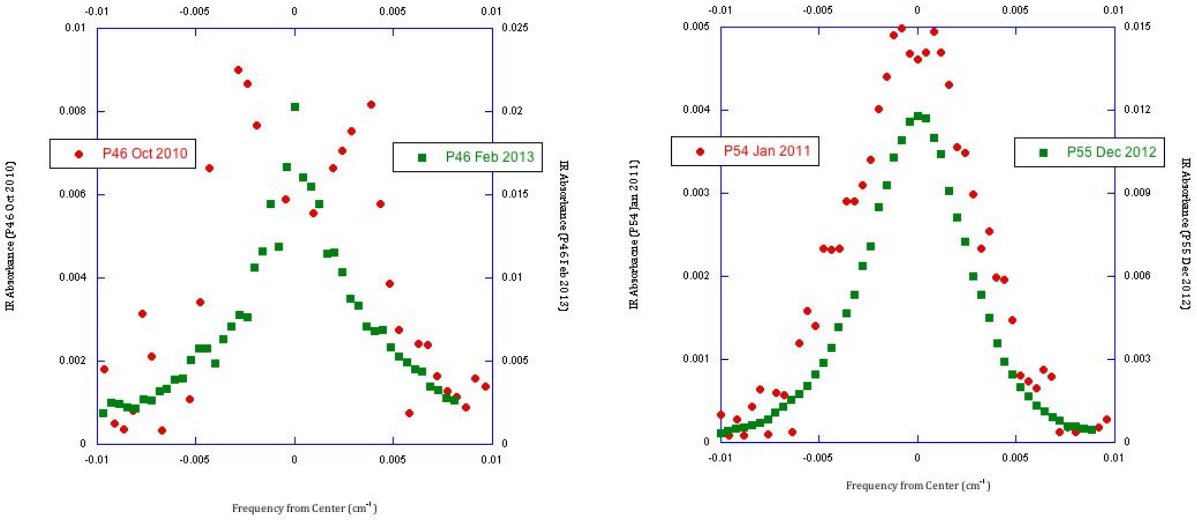

Figure 3.5 Two comparisons of line width spectra from close J states recorded by Kim et al and by the author. The horizontal axis, representing the frequency dimension are equilvalent in each plot. The right vertical axis represents the absorbance for the green traces from this work. The left vertical axis represents the absorbance for the red traces from Kim et al. Note the single Gaussian line shapes indicating only in-scattering for spectra collected by the author opposed to the double Gaussian shapes as collected by Kim et al.

Double Gaussian line shapes were observed by Mullin and coworkers[4] in a similar collision dynamics experiment between CO_2 and pyrazine. They recorded noticeable out-scattering beginning at the J=38 state. Using the Boltzmann distribution at room temperature and statistical mechanics, the relative population of CO_2 in J=38 is 0.87%.

$$P_i = \frac{(2J_i+1)e^{-\beta hc\tilde{B}J_i(J_i+1)}}{q^R} \qquad (3)$$

Here P_i is the relative population of molecules in state J_i, h is Planck's constant, c is the speed of light, $\tilde{B}$ is the rotational constant and q^R is the rotational partition function. For N_2O the relative population in state J=37 is 0.88%. With this study as a base, double Gaussian line shapes should begin to be recorded for N_2O at about J=37 not J=56 as reported by Kim et al. Revealing the correct line shape for the mid J states in the N_2O - pyrazine system is an important contribution of this work.

III. Summary

The mid J states line widths have of the N_2O-pyrazine system have been collected by IR transient absorption. Analysis of the line widths and conversation to translational temperatures showed with J>47, T_{trans} is linearly related to J state. The linear relationship is caused by a constant impact parameter for those collisions. With J<47 T_{trans} is stable at about 450K implying these molecules are scattered in by glancing collisions with a larger impact parameter. The T_{trans} will be used in further measurements on the pyrazine-N_2O system to develop P(E´,E)

Line shapes for each J state measured were single Gaussians not double Gaussians as observed previously by Kim et al. Because of defective equipment the line shapes in this

work are correct. Comparisons with studies by Mullin and coworkers on the pyrazine-CO_2 system leads us to expect that double Gaussian shapes will be measured starting with J=37.

References

1. Mullin, A. S., Micheals, C.A.,Flynn, G.W. (1995) *J. Chem. Phys.* **102,** 6032.
2. Kim, Kilyoung. Ph. D. Dissertation, Brigham Young University, UT, April 2011.
3. Sevy, Eric T., Rubin, Seth M., Lin, Zhen, Flynn, George W; (2000) *J. Chem. Phys.* ***113,*** *4912.*
4. Havey, Daniel. K., Du, Juan, Liu, Qingnan, Mullin, Amy S.; (2010) *J. Phys. Chem. A* ***114,*** 1569

Chapter 4:

Experimental Technique Guides for IR Transient Absorption

Chapter 4: Experimental Technique Guides for IR Transient Absorption

During the process of collecting the mid J state line widths and analyzing the data I have optimized many of the experimental procedures. These improved techniques will be valuable to future members of the Sevy research group to perform IR transient absorption experiments with the best results. Each procedure is designed to reduce labor costs, improve transient absorption signal intensity or reduce noise and error. Other scientists using IR transient absorption may also find these techniques useful as a troubleshooting guide.

The chapter is organized with each technique in its own section. The sections are loosely ordered by when the task would occur if the reader were setting up an IR transient absorption experiment. For example the section covering IR Diode Alignment (IV) is prior to the section on Data Treatment (XI). The final section (XIII) details the steps that should be taken in the near future to complete the mid J state measurements and enable low J state measurements.

I. Vacuum System

IR transient absorption experiments require mTorr range pressures to operate properly. To achieve these low pressures we use a custom glass diffusion pump. The diffusion pump is backed by an Alcatel rotary vane mechanical pump. Following correct operational procedure for the diffusion pump is critical to maintaining low vacuum. Figure 4.1 shows a photo of our diffusion pump and labels the inlet, output and rough pump valves. The valve configuration depends on the operating mode. During a line scan experiment, the inlet and output valves should be open with the rough pump valve closed.

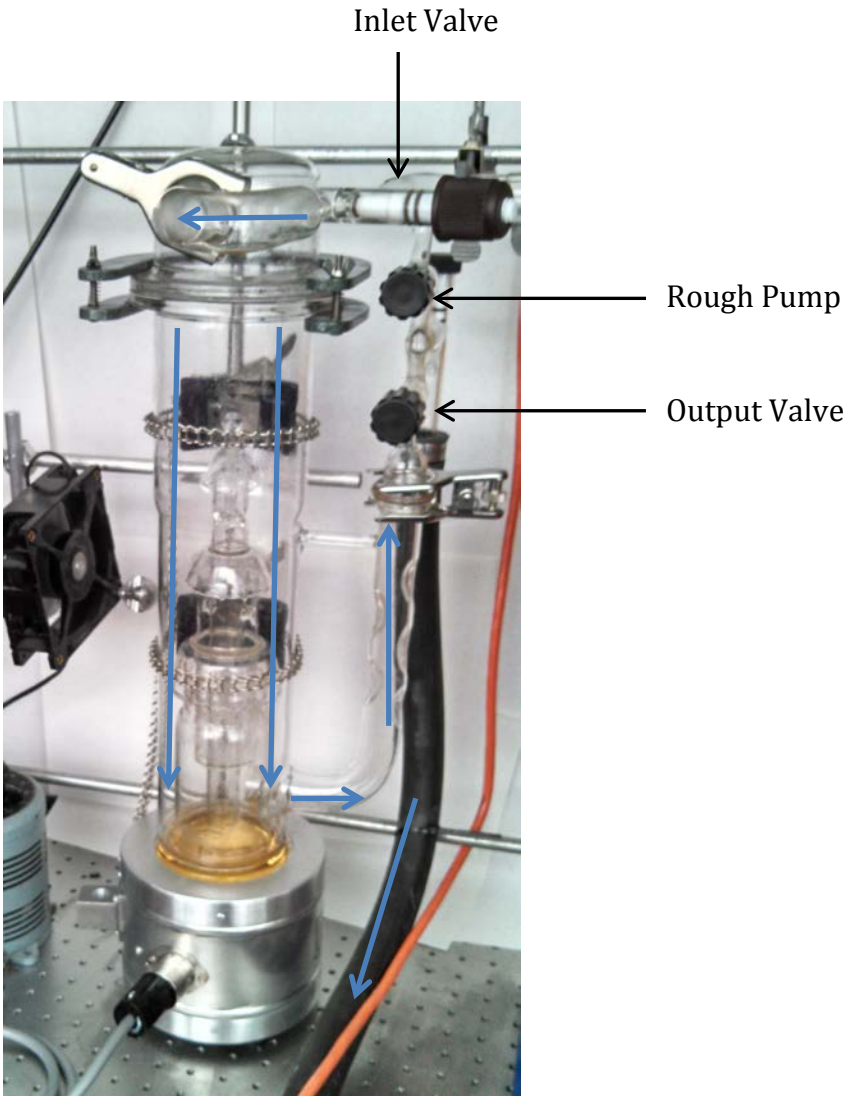

Figure 4.1 Our custom glass diffusion pump. The position of the inlet, output and rough pump valves for different vacuum situations is described in the text. The blue arrows in this picture show the direction of gas flow when the pump is operating. Gas enters at the top of the diffusion pump through the inlet valve is pulled down and around the outside of the Christmas tree structure and out at the bottom. Gas then flows through the large black hose connected to the Alcatel rotary vane pump (not shown) and out to the building air handlers.

If the system is going to be exposed to the atmosphere, the inlet valve should be closed with the output valve open and the rough pump valve closed. This will ensure that the diffusion chamber maintains vacuum and the silicon oil continues boiling, allowing the rest of the system to be worked on. This valve configuration is used when cleaning the sample cell windows or refilling the gas reservoirs. To restore vacuum to the system, the rough pump should be used first to decrease the pressure to about 200 mTorr. Close both the inlet and output valves for the diffusion pump and open the rough pump valve. Once the system reaches 200 mTorr the diffusion pump can be engaged by closing the rough pump valve, opening the output valve, and then opening the inlet. Experiments can be performed 8 hours after establishing a vacuum, which allows for any off gassing.

Since we operate at mTorr range pressures, a small amount of gas contamination can represent a large percentage of the total gas in the cell. The N_2O purchased from Intermountain Airgas is 99.999% pure and can be used without further purification. The pyrazine is a solid from Sigma Aldrich and may contain trapped atmospheric gases that must be removed by at least three freeze-pump-thaw cycles. About 1 g of pyrazine is stored in a bulb with a cold finger connected to the vacuum system. With the pyrazine in the bulb, a cycle consists of first immersing the cold finger in LN_2 and opening the valve on the bulb to evacuate the chamber. Second the LN_2 is removed and the valve is closed. The bulb is left to warm to room temperature before repeating the procedure. Pure samples will last for approximately 2 months of experimentation before completely subliming.

Flowing atmospheric gases, specifically oxygen, through the diffusion pump degrades the silicon oil. The oil is oxidized gradually with each exposure and darkens. Oxidized oil has a higher boiling temperature to maintain effective pumping action. The oil

can be used for years and should be replaced when it approaches a caramel color with Dow Corning #704 Diffusion Pump Fluid. We commonly purchase new oil but the used oil can be recycled by vacuum distillation with concentrated effort. To replace the oil the pump must be cooled, disassembled, cleaned with a solvent, reassembled, and warmed under vacuum before operation can be restarted.

During an experiment the N_2O and pyrazine need to continually flow to through the sample cell at the proper pressure so that each laser shot encounters new gas. Inaccurate pressures will introduce error in the rate constants of the collisional energy transfer. To prepare the sample cell, measure the UV power before and after the cell with it still under vacuum. The operation of the UV excimer laser is described in section II. These measurements record the UV power lost when passing through the CaF cell windows. Close the three back valves so that any gas released from the bulbs is forced to flow through the sample cell and out the diffusion pump. Set the pyrazine needle valve to 0.15 and the N_2O needle valve to 0.30. Fill the flow cell with 10.0 mTorr of pyrazine by opening the valve on the pyrazine bulb and adjusting the MKS solenoid controller setting. Measure the UV power after the cell with the 10.0 mTorr of pyrazine. Next flow in 10 mTorr of N_2O by opening the valve on the N_2O bulb and adjusting the solenoid. The total pressure should now be 20 mTorr. Measure the UV power after the cell with both the pyrazine and N_2O. Since N_2O does not absorb 248 nm light the power reading should be the same as that with only pyrazine in the cell. If the power is lower the pyrazine concentration has decreased and if it is higher the concentration has increased. Tune the solenoid valves appropriately for a 1:1 mixture of pyrazine and N_2O, using the UV power to monitor the

pyrazine concentration. Once the concentrations are set, the sample cell is ready to record line shapes and line widths.

II. Excimer Laser

An important aspect of excimer laser maintenance is to always record the pressure in the lasing cavity and the internal power each day the system is turned on. Having a record of the laser power will clearly illustrate the decrease in power as the gas mixture decays. New gas fills should be used whenever the laser has been idle for more than two months or if the internal power drops down below usable levels. The usable level in our setup is an internal reading of about 150 mJ. To refill the gas in the lasing cavity refer to the standard operating procedure in the laser lab notebook.

The excimer laser is operated by the excimer.vi Labview program. This program will fire the laser at 3 Hz, 5 Hz, or allow it to be externally triggered and perform the new fill procedure. When aligning the UV laser it is useful to use one of the faster firing rates. During an experiment the laser should be on the external trigger setting and will be controlled by the DDG, see section VIII, at a fire rate of close to 1 Hz. If the excimer laser will not fire from the Main1.vi program, refer to section VII, it is most likely because the laser is not in external trigger mode. Most of the other features of the excimer program are not used in normal operation for line center and line scan experiments.

The UV power at the sample cell is in the optimum range between 2-4 mJ/cm^2. This corresponds to 40-50 mV as measured with a Gentec Powermeter Qe25SP and a beam diameter of about 7 mm. There should be enough UV photons so that all of the pyrazine in the beam path is excited, after overcoming losses from sample cell windows, but not enough photons for two photon absorption to occur. Two photon absorption begins

occurring at 9 mJ/cm^2, well below our operating conditions. The laser power can be reduced using the Brewster stack if it is too high. Brewster windows should always be added to the stack in pairs at a right angle to each other, to prevent displacing the beam path and disrupting alignment further along in the system.

UV laser alignment is simpler and should be performed after collimation and alignment of the IR diode beam, refer to Section IV. When aligning the UV laser, first align by eye through the irises on the long or sample side of the optical table. Since the human eye only senses the fluorescence from the UV laser exciting the dye molecules in the white card, it is more accurate to use the power meter once the rough alignment is complete.

The alignment procedure for the UV laser is detailed in Figure 4.2. Place the power meter behind iris (1) and maximize the signal using UV alignment mirror (a). Move the power meter to behind iris (2) and maximize the signal with mirror (b). Repeat these steps in an iterative fashion until the alignment is completed. Improving the UV alignment increases the number of excited pyrazine molecules and thus increases the number of energy transfer collisions and the intensity of the transient signal.

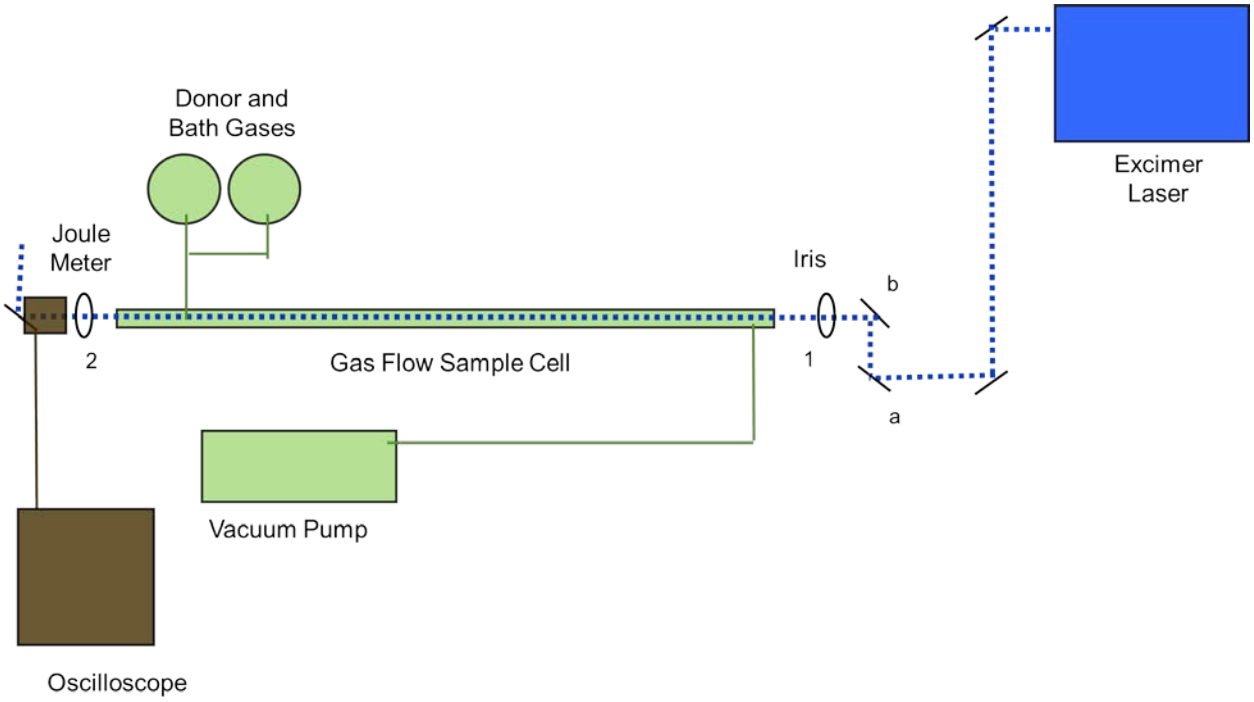

Figure 4.2 Aligning the excimer laser with the power meter involves iterating between two positions. With the power meter behind of iris "1", maximize the signal using the UV mirror labeled "a". Then move the power meter to behind iris "2", as shown in the diagram, and maximize the signal using the UV mirror labeled "b". This diagram has been simplified from the experimental setup in Chapter 2, Figure 2.#. The sample cell is often removed for alignment but is present in the figure to orient the viewer.

III. InSb Detectors

Before each experiment, the detectors should be the first instrument powered on and cooled. We found that it requires close to an hour before the ground current stabilizes after filling the internal dewars with LN_2. During the cool down time other parts of the experiment can be readied, like flowing the N_2O and pyrazine gas, see section I, and etalon calibration, refer to section VII. After the ground current has stabilized the detector reservoirs should be kept full to avoid further changes in the temperature and ground voltage.

The preamplifier batteries are an important element to check if no IR signal can be detected. Whenever there is no IR signal, always check if something is blocking the beam path. Then if IR signal was present the previous day and no changes have been made to the IR alignment, replace the preamplifier batteries. The preamplifiers require each battery to hold voltage greater than 10 V to function. The voltages can be measured with a multimeter, but the best way to check for bad batteries is to replace them.

IV. IR Diode Alignment

Proper IR diode alignment will reduce laser jitter and increase the transient signal. Figure 4.3 diagrams the alignment process for the IR diode. To align the IR laser first move a detector to behind the pair of irises (1,2) just in front of the diode rig. If the IR beam is not collimated, a lens may be needed to focus the light onto the detector for an appreciable signal. Center the irises (1,2) along the beam path and then remove the detector. Next align the HeNe laser along the same irises (1,2) using only the HeNe mount (a) and the removable magnetic mirror (b). Now that the two lasers are on the same beam path, use the visible HeNe laser to adjust the rest of the mirrors (c-j) so that the beam will travel the

length of the table. This will also align the IR diode along the same path. Remove the HeNe and place the detector behind the irises (3,4) in the sample leg of the experiment. Center the sample leg irises (3,4) on the IR beam. Insert the HeNe and align it to irises (3,4) with only the HeNe mount (a) and the magnetic mirror (b). Refine the HeNe and IR laser alignment with mirrors (c-j). The IR should hit the center of each mirror and the sample leg should be at the same height as the monochromator slits.

Once the laser is aligned it needs to be collimated. Collimating the beam can be a difficult process without a known starting point. I decided to place the detector at the end of the sample cell path and adjust the lens so that the signal was maximized. This means that the beam is now focusing onto the detector. Move the lens is towards the diode rig to collimate the beam. To test for collimation, insert extra irises in the beam path, center them, and record the beam diameter. A collimated beam will be the same diameter along the entire path. Make careful adjustments to the lens until the IR beam is collimated. A properly aligned and collimated diode beam will have more intense transients and less noise from laser jitter.

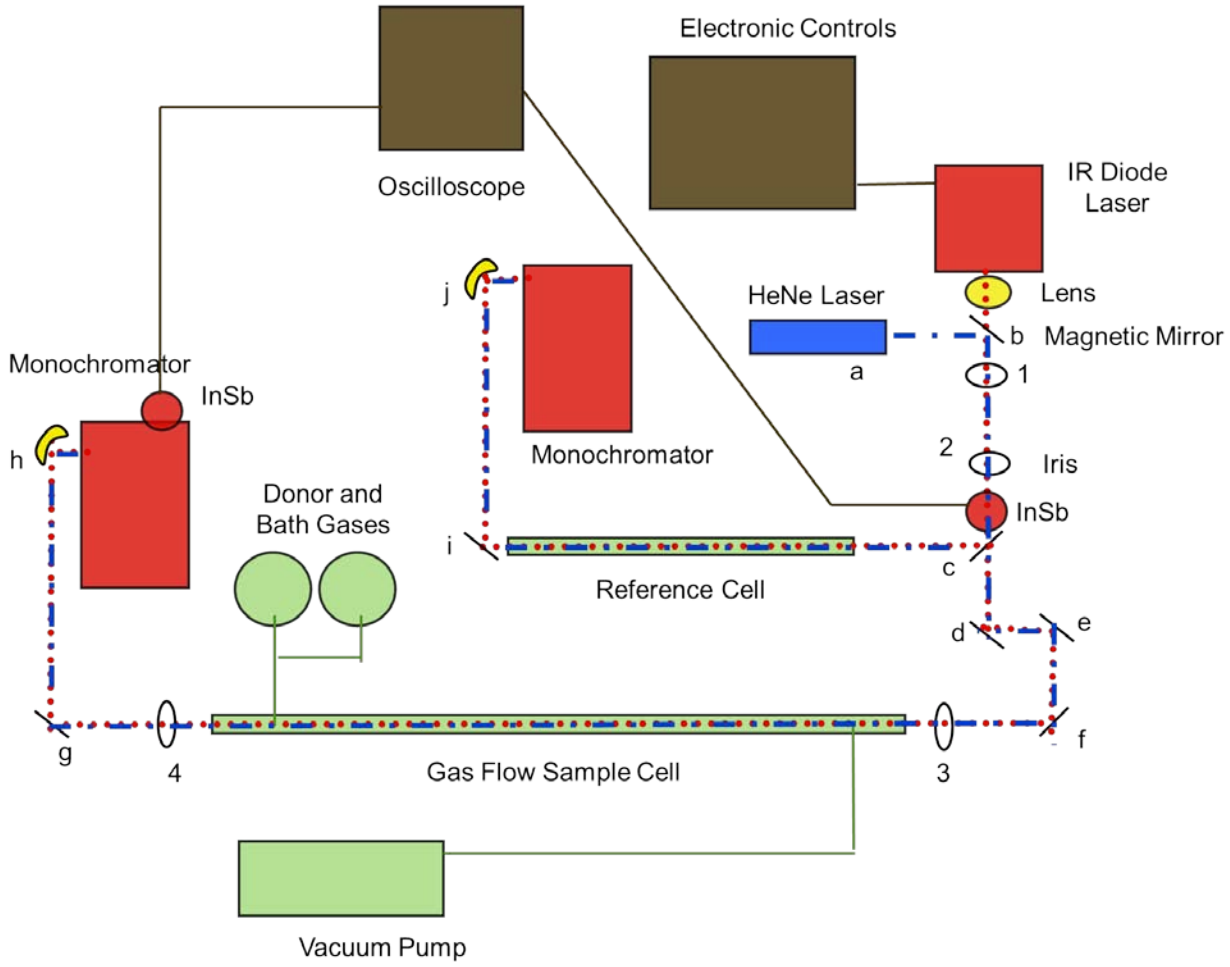

Figure 4.3 The mirrors, iris and beam path for aligning the IR diode is shown here. Although the HeNe laser appears red to our eyes it is shown in blue here because it is more energetic than the IR beam. The procedure for the full alignment is found in the text. In short, we use the irises to define the IR beam path and align the HeNe mirror along that path. With the beams matched we can adjust other mirrors using the visible HeNe and know that the IR diode beam will follow these changes in the beam path. As with the UV alignment the sample cell is often removed for IR alignment but is shown here for context.

V. Monochromators

The most common difficultly with the Acton SP series monochromators is controlling the grating position. We have used an HP 486+ RPN graphing calculator supplied by Acton with a serial connection and Acton programing to drive the grating. This setup works excellently when the program installed, however, the program can be accidently erased, and the calculator becomes useless. The program and installation guide has been transferred from the original floppy disk to a CD-ROM kept with the manuals for the monochromator. The most difficult part will be finding a compatible computer to install the program. The installation the program is DOS based and requires a 32-bit based Windows computer with a serial port. In the future, the Sevy research group may need to consider running the monochromator with a Labview program.

Calibrating the monochromators will ease peak finding and IR diode calibration, see section VI. The grating angle is controlled by a setting on the HP calculator which is displayed in the approximate nanometer wavelength of light passed by the monochromator. We calibrate the monochromator with the HeNe laser to find a more exact wavelength passed by the instrument. A calibration curve is constructed from measuring the calculator setting which passes the fundamental HeNe beam at 632 nm and higher order reflections. This curve is helpful to correlate diode temperatures and currents to frequency settings.

VI. Finding and Identifying N_2O Peaks

Each diode must be calibrated before it can be used to collect IR transient absorption spectra. The frequency of light emitted from lead salt diodes is dependent on the operating temperature and the applied current. These settings are not correlated to wavenumber by the manufacturer. Calibrating the diode consists of comparing the known spectrum of N_2O to the observed spectral features at a particular temperature and current, finding a match and recording the frequency.

The calibration process is described as follows. With about 100 mTorr of N_2O held static in the sample cell, the monochromator is tuned to a wavelength corresponding to a P branch transition of the $00^00 \rightarrow 00^01$ ro-vibrational transition. Then the diode is set to a modulation intensity of around 20mA, the lowest possible temperature, and scanned through the possible current range looking for prominent absorption peaks. It is important to start at the lowest possible temperature because mode hopping and frequency jitter is reduced at lower the temperatures. Once a good spectral region is found with several visible peaks, a solid Ge etalon is placed in the reference line. At this point the signal from the detector on the ocilliscope will look similar to Figure 4.4. The distance between each peak is measured in units of etalon fringes. Then these distances are used in the findpeakN_2O.vi Labview program to find possible matches by comparison with the HITRAN database. Matches from the Labview program are then compared visually until an exact spectral match is found. Figure 4.5 shows the correct correlation with a computer-generated match and the observed N_2O absorbance spectrum.

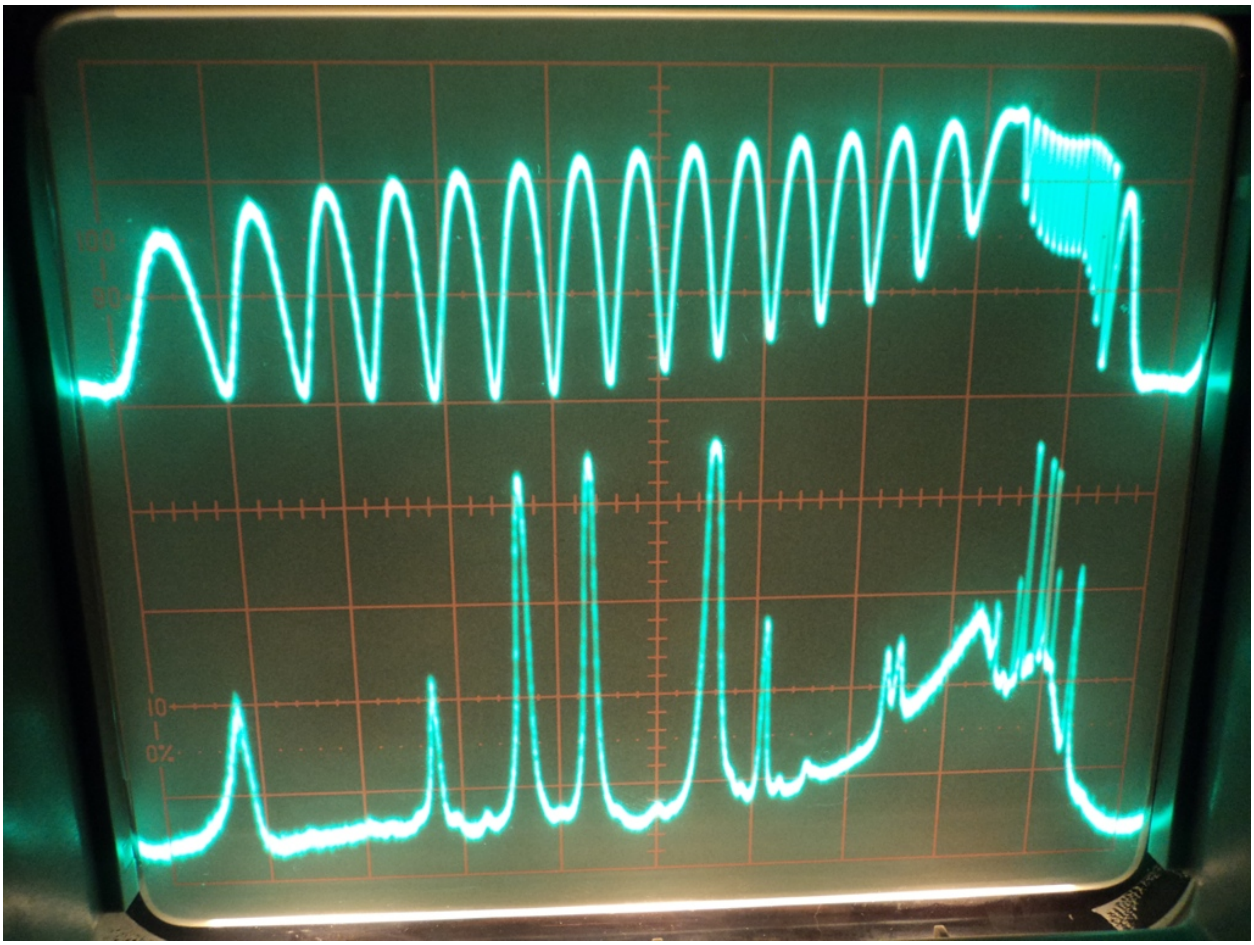

Figure 4.4 A picture of the oscilloscope screen while finding the N_2O transitions in frequency space. The bottom trace is the IR absorbance on the measurement line showing the N_2O peaks. The top trace is the Ge etalon interference pattern. The distances between the peaks are measured in etalon fringes and used in the findpeakN2O.vi program.

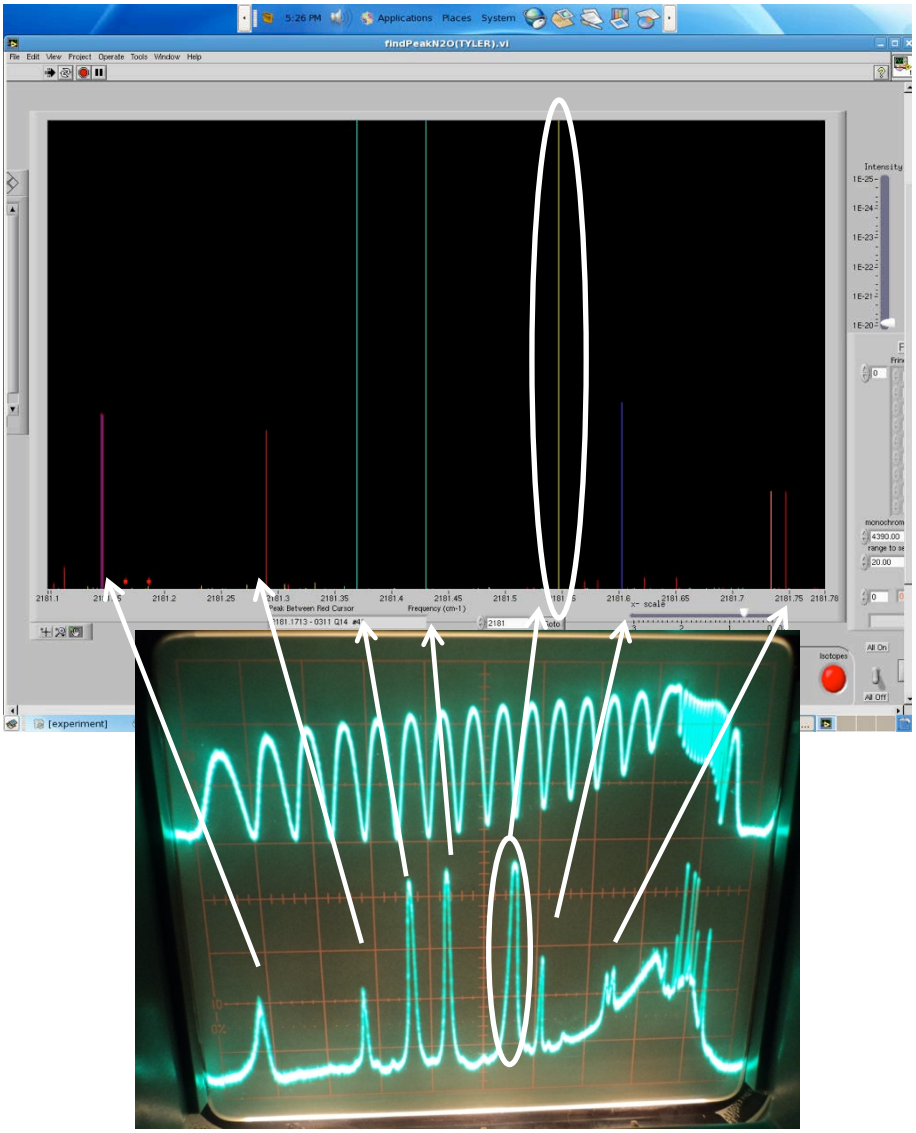

Figure 4.5 A screenshot (top) of the findpeakN2O.vi program and the proper peak correlation for the absorbance spectrum (bottom). The 00^00-00^01 P43 transition is the circled line in both images. The colors for different lines in the findpeakN_2O.vi program represent different vibrational transitions of N_2O. This transition at 2181.5465 cm^{-1} is now calibrated with IR diode set to 85.50 K and 271.7 mA. The monochromator was set to 4587.00 nm during this calibration.

The monochromator is then tuned to a different wavelength and the process is repeated. The IR settings and spectral region are recorded for future use during line shape and line center experiments. Our goal is to locate as many peaks as possible in P-branch of the 00^00-00^01 transition.

VII. Fabry - Perot Etalon Calibration and Hysteresis

The calibration of the scanning etalon has a pivotal role in line shape measurements. If the frequency axis is not well-defined then the widths and thus the temperatures will also be in error. The Main1.vi Labview program is used to drive and calibrate the etalon. First, center an etalon fringe on any known peak in the IR spectrum. It may be easier to set the DAC step (Digital to Analog Convertor) to 2000 and use the zero knob on the control box to center the fringe. Lock the fringe by activating the lock-in amplifier, record the DAC step, and drive the etalon to the center of a nearby peak. Input the starting DAC value the final DAC value and the frequency difference into the Main1.vi and calculate the frequency per DAC step. I have adjusted the gain on the etalon control box to its lowest setting and a normal calibration value is close to $2x10^{-5}$ cm^{-1} per DAC step. Because of its importance, the calibration value is remeasured in the opposite direction. Unlock the etalon fringe, recenter it on the final peak, lock the fringe in the new position, and drive to the starting peak. The frequency per DAC value should be within $5x10^{-7}$ while the actual DAC numbers may have changed slightly. This is because the etalon has a small lag when it changes direction. This hysteresis effect is accounted for during data analysis, see section XI.

At the beginning of my work in the Sevy lab, the hysetersis effect was large enough that the peaks of each pass was separated by more than 0.004 cm^{-1} during a line scan experiment, see section IX. This malfunction may have been occurring for months prior to my experiment. We believe it is one of the main causes for the incorrect double Gaussian line shapes observed by Kim et al. Refer to Chapter 3, section II for a more detailed discussion of this issue. To troubleshoot the etalon, I measured the current and voltage of all the electrical connections. The voltage output from the computer to the etalon controller box will vary linearly with the DAC value. The current entering the etalon from the controller should change linearly with the DAC steps, while the voltage remains constant at 12V. During troubleshooting I used the scanner.vi program to drive the etalon without any of the other experimental systems running. The scanner.vi program is a sub-program of the Main1.vi program and can be accessed easily from the Main1.vi program.

Measuring the voltage from the computer to the controller box an oscilloscope revealed it was linear with the DAC setting and therefore not the cause of the problem. To measure the current passing from the controller box to the etalon I stripped a BNC type coaxial cable and spliced the shielding together, leaving the core wires loose. This cable is pictured in Figure 4.6. With a multimeter completing the circuit, I could measure the current with respect to the DAC setting. I found a nonlinear change in the current with relation to the DAC steps.

To mitigate the electrical interference I, grounded the metal surface of the experiment table and replaced the etalon cable with a brand new quad shielded coax cable. The current had been leaking out of the cable and into the metal surface of the table causing large hysteresis effects. I also observed that BNC connections should not be

allowed to touch the table. The power meter connections, detector connections, and the etalon connection all leaked current out to the table through the metal fittings. To solve this I placed each connection on a kitchen sponge insulating it from the metal surface. Replacing the cable and insulating the connectors caused the hysteresis effect to decrease dramatically in our experiment setup.

Preventative maintenance should be performed on the etalon to conserve its internal vacuum. If the pressure increases the fringes become hazy, or less sharp. Hazy fringes affect the calibration because it is more difficult to align the fringe with the center of the peak. Since the vacuum leaks very slowly over time, it is unlikely there will be a sudden change in the appearance of the fringes from one day to the next. Vacuuming out the etalon at least once every year will ensure a low vacuum, sharp fringes, and good calibration.

Figure 4.6 The spliced coaxial BNC cable for measuring the current flow to the scanning etalon. At the open end on the right, the cladding has been joined together in the red wire tie and wrapped in electrical tape. The center core is left bare to connect to the multimeter and read out the current.

VIII. Digital Delay Generator and Timing

We discovered a problem with the digital delay generator, abbreviated DDG at the beginning of our line width measurements. The DDG manages the timing of the excimer laser pulse relative to the 1000 Hz modulation cycle of the diode. It also has secondary connections to the IR spectrum, the etalon fringe and the lock-in-amplifier. Figure 4.7 illustrates the timing of all of these different signals. The fault in the DDG was an inconsistent delay for multiple laser shots. Variable delays in the excimer firing would result in unacceptable variation in time zero. If we attempted an experiment with the defective DDG there would be large noise contamination. The defective DDG may also have had a large influence on the line widths collected by Kim et al.

We replaced the DDG and optimized the timing of the new instrument. The most intense transients with the largest total absorbance requires the excimer to fire at the center of each modulation cycle. In order to obtain a 1 Hz excimer fire rate the DDG must trigger off of one IR diode modulation cycle, wait 1 second plus a specified number of nanseconds before sending the signal to the excimer to fire. The additional nanoseconds center the excimer pulse in the modulation cycle. To find the additional wait time, first align a transition with an etalon fringe and engage the lock-in-amplifier. The phase setting on the lock-in-amplifier can influence the timing and should remain fixed after optimizing the DDG timing. By firing the excimer laser and observing the change in the transient intensity, we tuned the DDG to the proper delay setting of 550 ns.

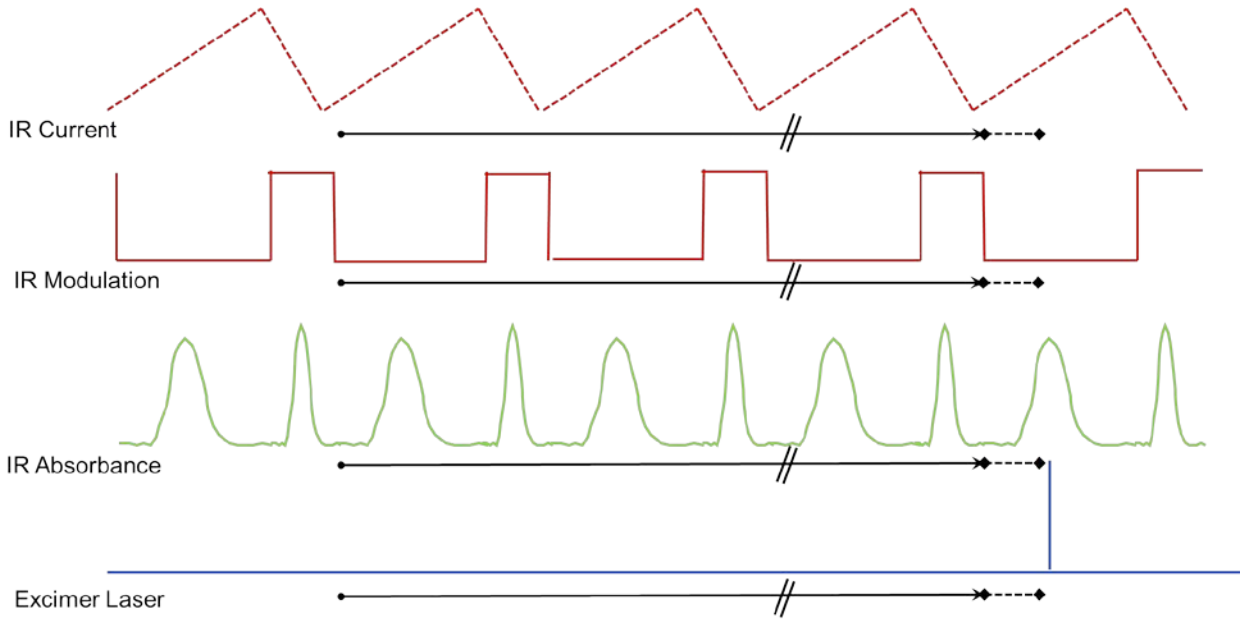

Figure 4.7 The timing of several experimental signals. The top line is the IR current which increases linearly from the base by a user defined amount while the modulation signal, red solid line, is negative. When the modulation changes sign the IR current decreases linearly back to the initial value in a shorter space of time. This cycle is repeated 1000 times a second. Changing the diode current changes the frequency of the beam and an IR absorbance spectrum, in green, is recorded by the detectors. The DDG timing is shown in black. It first triggers from a negative edge of the modulation cycle and waits 1 sec, shown by the solid arrow. After 1 sec the modulation cycle is back to a negative edge and the DDG waits an additional 550 ns, shown by the dotted line, before triggering the excimer to fire. The additional wait time is calibrated to fire the excimer at the center of the increasing diode current and the center of the absorbance peak. The result is an excimer fire rate of 1 Hz at the center of the IR modulation cycle.

The DDG timing has also proven to be a factor in the shape of the pre-trigger line widths. By changing the relative timing of the UV laser pulse with respect to the diode modulation cycle I could alter the shape of the pre trigger line width. Figure 4.8 charts three pre-pulse line widths at different DDG times. The largest IR transient signals occur at a delay of 550 ns when the UV laser fires exactly in the middle of the modulation cycle. If the UV laser fires too late, meaning longer delay times, the negative dip feature appears on the positive side of the line width scan. If the UV laser fires too soon, meaning shorter delay times, the negative dip feature appears on the negative side of the line width scan. With the DDG powered off, meaning the delay is now zero, the negative feature is still present. Even though the timing affects the pre trigger shape, the DDG is not causing the deviation. Furthermore, when these tests were performed on P48, the 1μs absorbance line width was not statistically different between different delay settings. The interesting pre-pulse shape is as yet an unexplained phenomenon, but does not appear to have an impact on our ability to find the 1 μs line widths and determine P(E´,E).

IX. Line Scan Experiment

Line scan experiments require that all of the instruments and pieces discussed previously work in concert with one another. Initially the equipment is all turned on and the detectors cooled while the sample cell is readied. Follow the procedure in Section I to prepare the sample cell. Once the cell is ready, the IR diode can be tuned to the frequency of the desired peak which was found in the calibration process described in section VI.

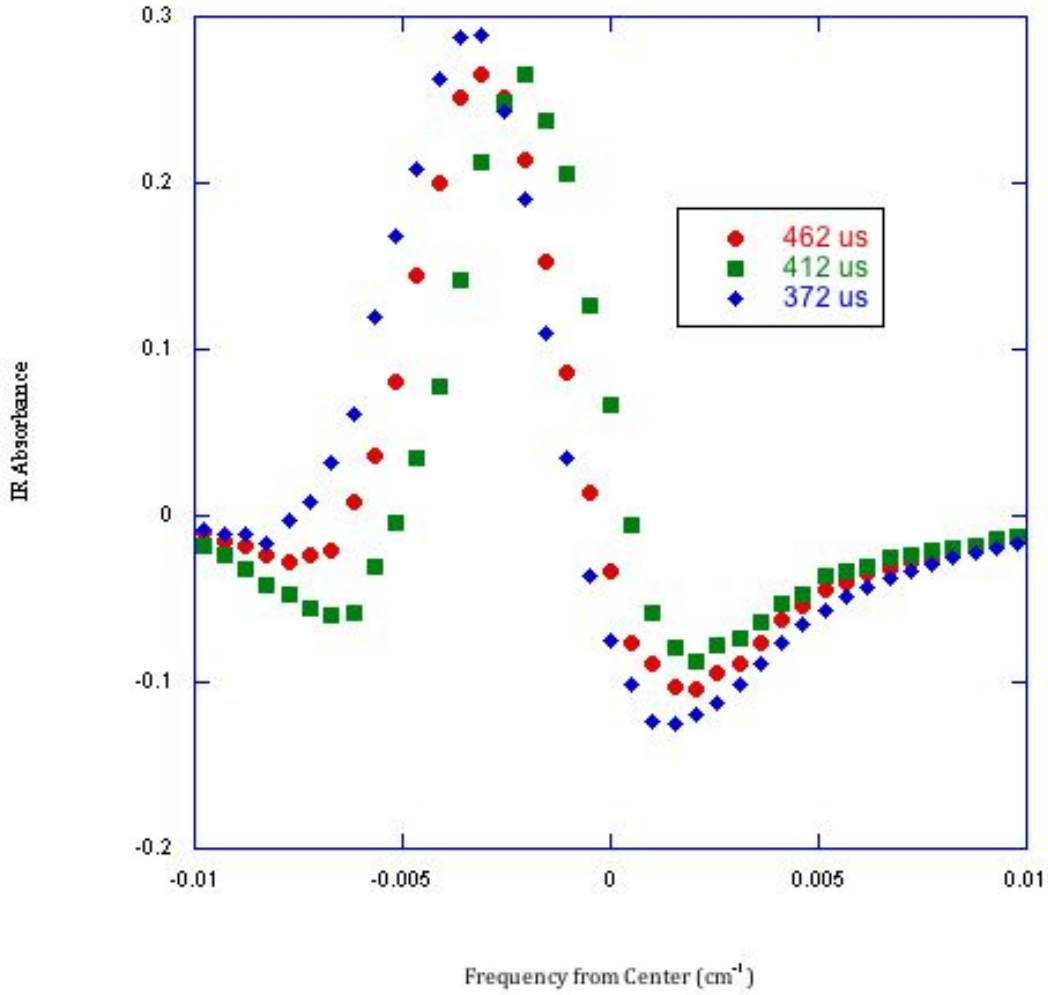

Figure 4.8 Pre-pulse line widths at shorter delay times. The negative dip feature changes position relative to the peak due to the DDG delay. At short delays the dip appears after the peak or at positive frequencies. Longer delays shift the dip towards negative frequencies. The maximum absorbance occurs with a 552 μs delay where the peak and negative feature overlap producing dips on either side of the peak.

The etalon is then calibrated using the procedure in section VII. After the etalon and diode are ready, decrease the diode modulation amplitude to 0.2 mA, center the etalon fringe on the desired $00^00 \rightarrow 00^01$ rovibrational transition and record the DAC position in the Main1.vi prgram. The DAC range should be 1000 DAC numbers centered around the peak position. Load the proper saved settings for recording a line shape on the digital ocilliscope, as described in section X. Lock the etalon fringe to the modulation cycle and drive the etalon to the starting position. While driving to the start position, fire the excimer laser and adjust the scope voltage settings so that all the traces remain on the screen. Start the linescan.vi program from inside the Main1.vi program and complete the boxes for file name, peak, number of shots, and number of passes. Also check to confirm that the DAC range and DAC calibration values are correct. Use the preamplifier adjustment screw to zero the ground signal on the measurement detector. Finally, click the "Start" button on the linescan.vi program. The program will now average the specified number of transients for each of the given points in the line scan and complete all of the passes without further required inputs. Immediately after the program is finished the data can be analyzed.

X. Data Treatment

The first step in the analysis of the transients is to determine the absorbance at 1 μs after the UV laser fires. Inside of the linescan.vi labview program is the getpointbeta.vi sub program. Its function is to select out the proper points to form slices of the line shape before the laser pulse, at 1 μs after the pulse, and at 15 μs after the pulse. The pre-pulse and 15 μs line shapes are diagnostic. The 1 μs absorbance is found by fitting the transient from 0-6 μs to a line and then calculating the absorbance at 1 μs from the slope and intercept. Since we are most interested in the change in absorbance the initial pre-pulse

absorbance is defined as zero, which makes the intercept zero as well. Therefore the 1 μs absorbance, notated $A_{1\mu s}$, is calculated from

$$A_{1\mu s} = m \quad * 1\mu s + 0 \qquad (1)$$

where *m* is the slope of the transient fit from 0-6μs.

The length of the linear fit is critical to minimizing the impact of any noise on the slope. Figure 4.9 shows several linear fits for the same P55 transient displayed in Figure 3.1. The slopes of the different fits are: 0.0076 abs/s from 0-2 μs in green; 0.0103 abs/s from 0-4 μs in blue; and 0.0096 abs/s from 0-6 μs in yellow. Longer fit times are a better representation of the transient behavior. In all cases the fit cannot be extended too far or the increase in absorbance becomes nonlinear due to second and third collisions between N_2O and any other molecule.

If needed the linear fit length can be adjusted in the getpointbeta.vi sub program in the linescan.vi program. The parameter labeled "k" in the program will alter the ending point of the linear fit. With the current scope settings a value for parameter "k" of 200 would mean a fit length of 0 μs. To increase or decrease the fit length by 1 μs add or subtract 100 from the "k" parameter.

The k parameter corresponds to the index of the time values extracted from the digital scope. Therefore the scope needs to be properly set to export the correct number of points for each transient. If the scope math settings are changed, then the point at index 800 will not be at the time of 6 μs following the laser fire and the linear fit will not compute properly. The scope settings are saved in the scope memory and can be recalled.

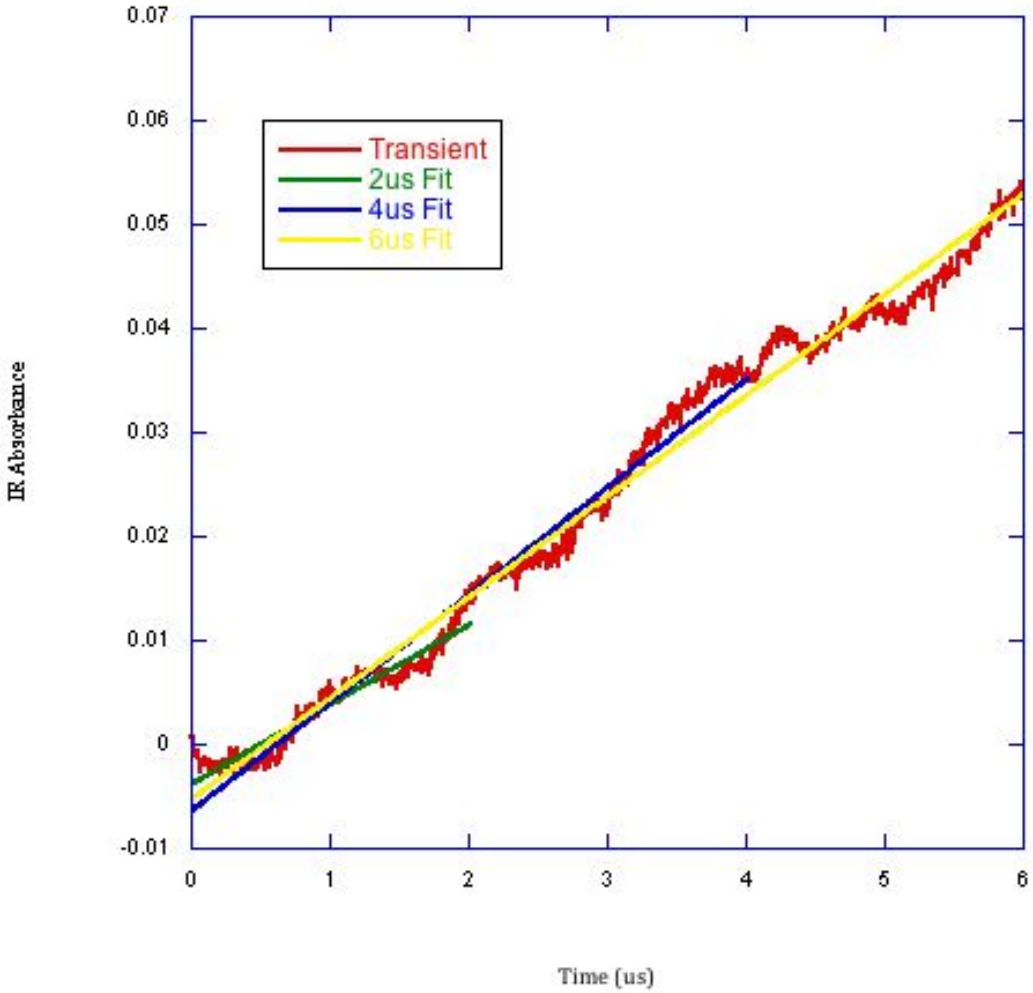

Figure 4.9 Three different linear fits for the transient in Figure 3.1 are plotted. The green fit is over 2 μs with a slope of 0.0076 abs/s; the blue fit is over 4 μs with a slope of 0.0103 abs/s; and the yellow fit is over 6 μs with a slope of 0.0096 abs/s. From this and many other transients we have concluded that longer fit domains better represent the data.

Save file #1 is for taking power readings of the UV laser beam and save file #2 is for line shape experiments. The correct scope settings for our experiment are also detailed in the side panel of the linescan.vi program in case the save files are corrupted.

Another element of data analysis is the treatment of the line shape from each pass. Four passes of the P55 line scan, a reproduction of Figure 3.2, are shown again in Figure 4.10 to emphasize the slight hysteresis in the scans. The peaks for the passes are not aligned together because of a small lag in the etalon when it changes directions, refer to section VII. Previously in our lab these passes were averaged together to form a single line shape. Averaging passes which are not perfectly matching in frequency space changes the FWHM. The better method is to treat each pass as its own experiment. Each pass is fit separately to the Gaussian function:

$$A_{fit} = a\left[exp\left(\frac{-4\ln(2)\,(x-b)^2}{\Delta\nu^2}\right)\right] + d \qquad (2)$$

Where the *a* term controls the amplitude of the curve, the *b* term adjusts the position on the x-axis, the *Δν* term is the FWHM, and the *d* term adjusts the position on the y-axis. The FWHM parameter from the Gaussian fit of each line is used to calculate T_{trans}.

$$T_{trans} = \frac{m_{N_2O}c^2\Delta\nu^2}{8k_B\ln(2)\nu_0^2} \qquad (3)$$

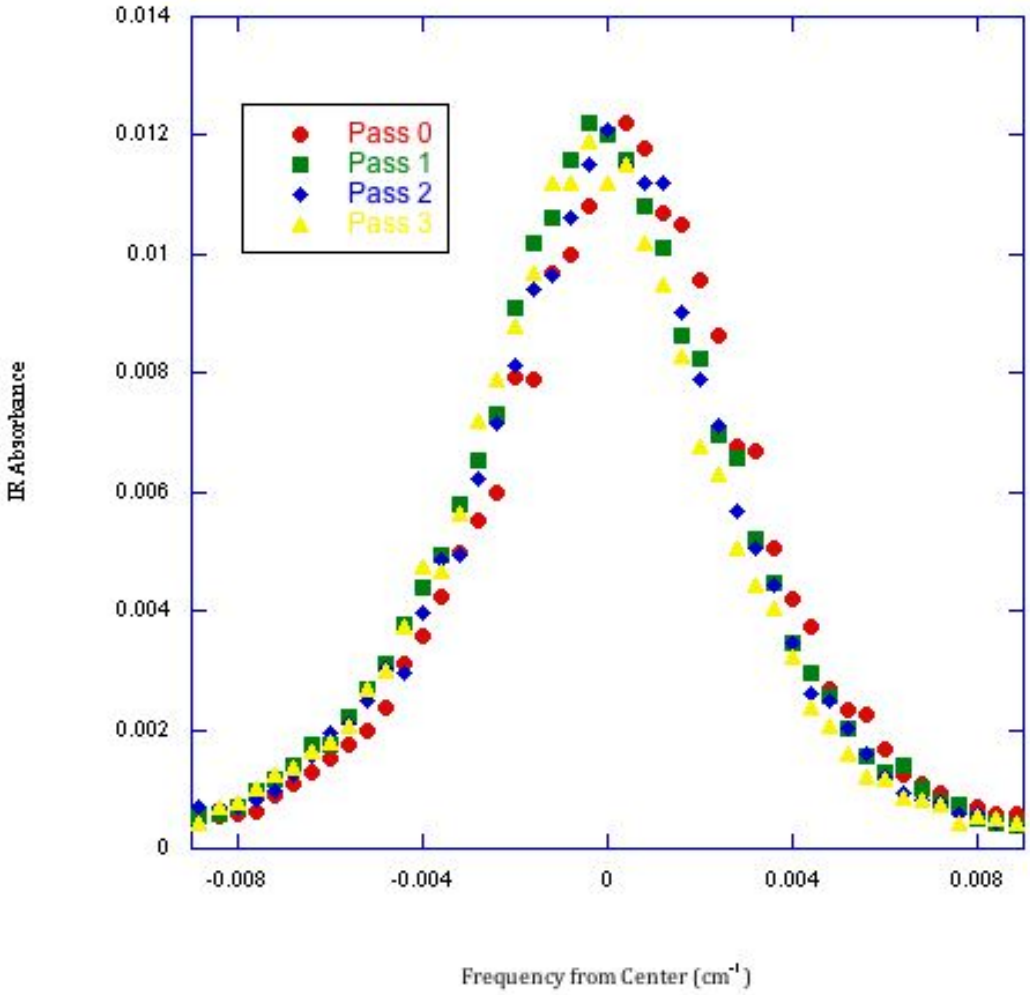

Figure 4.10 Four complete line widths of the P55 transition are shown. Each point represents a 1μs transient absorption signal, see Eq. (1). Pass 0 was measured beginning at low frequency and scanning in the positive direction. Pass 1 returned to the starting point and so forth. Notice the maxima are not all aligned because of a slight hysteresis in the scanning etalon.

In this equation, m_{N_2O} is the mass of N_2O, c is the speed of light, $\Delta\nu$ is the FWHM, k_B is the Boltzmann constant and ν_0 is the center frequency of the transition. Widths and temperatures can then be averaged together for multiple passes on different days for the same J state. This separate procedure ensures that any additional error is not introduce into the data by hysteresis. Table 3.1 lists each of the measured J states with their line widths and translational temperatures and Figure 3.3 plots the T_{trans} versus the J state. A full analysis of the data was not possible in this work because of time constraints. If possible, I would continue with measuring line centers, determining the rate constants and calculating P(E´,E). See Section XII for a description of future efforts to find P(E´,E) for the pyrazine-N_2O system.

XI. Laser Jitter

After measuring line widths for the mid J states, I began running line scan experiments on some of the low J states of the pyrazine-N_2O system. Figure 4.11 is a single pass of a P36 line scan. The noisy, cluttered appearance exemplifies the line scans for all the low J state line widths. These line widths did not fit a single or double Gaussian curve, and were not scientifically usable. To investigate the cause of the noise in these low J state line widths, I began by observing the raw transients. Since all further data analysis is built on the transient IR absorption, better transient signals would result in better line widths. Indeed the transient signals for the low J states were very poor. Figure 4.12 shows a transient from the center of the P36 line width in Figure 4.11. The noise oscillations dominate the signal. Using a linear fit to find the 1 μs absorbance value is not sufficient when the noise period is on the order of microseconds.

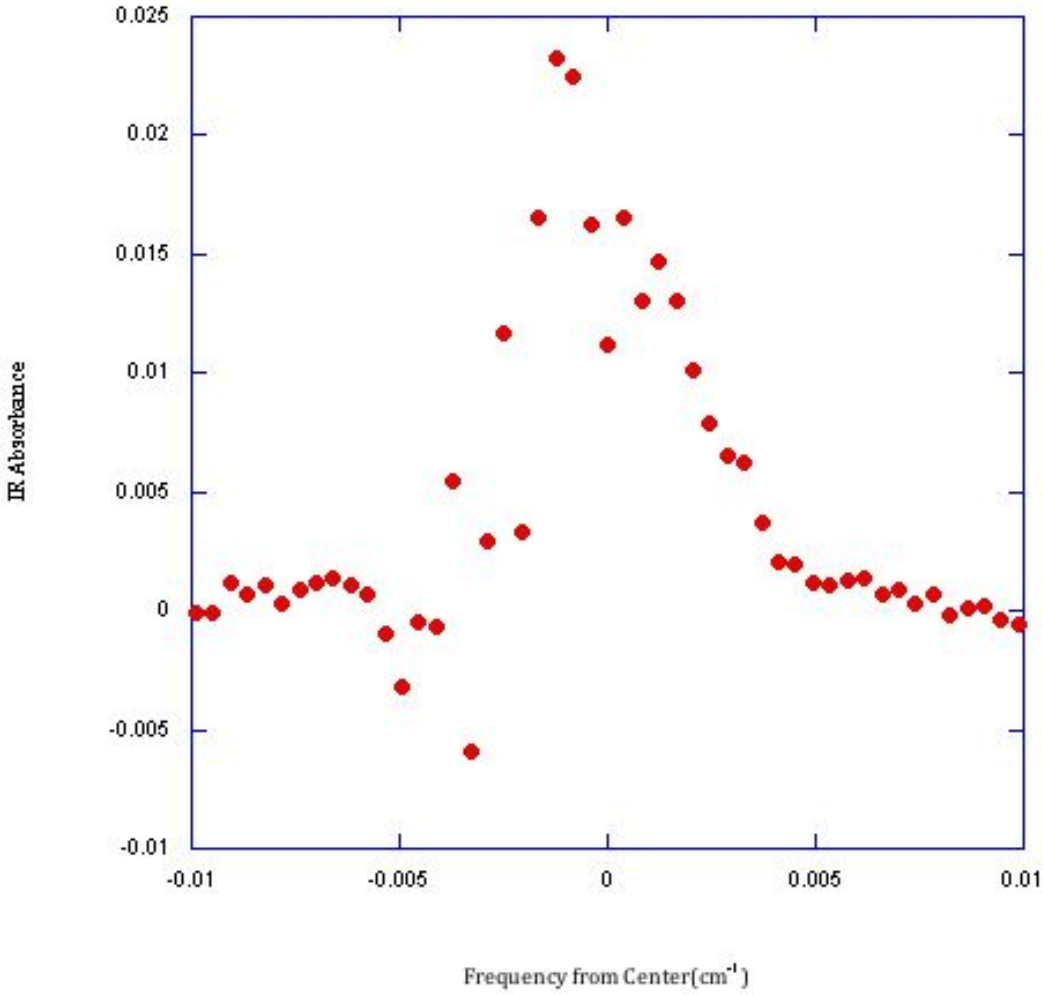

Figure 4.11 Pass 1 for a P36 line width scan. Note the negative dip on the negative frequency side of the peak similar to the pre-pulse widths, see Figure 4.7. The scan is less clean and was difficult to fit accurately to a Gaussian function. It and the other low J states scans were not usable because of the large amount of noise in the spectrum.

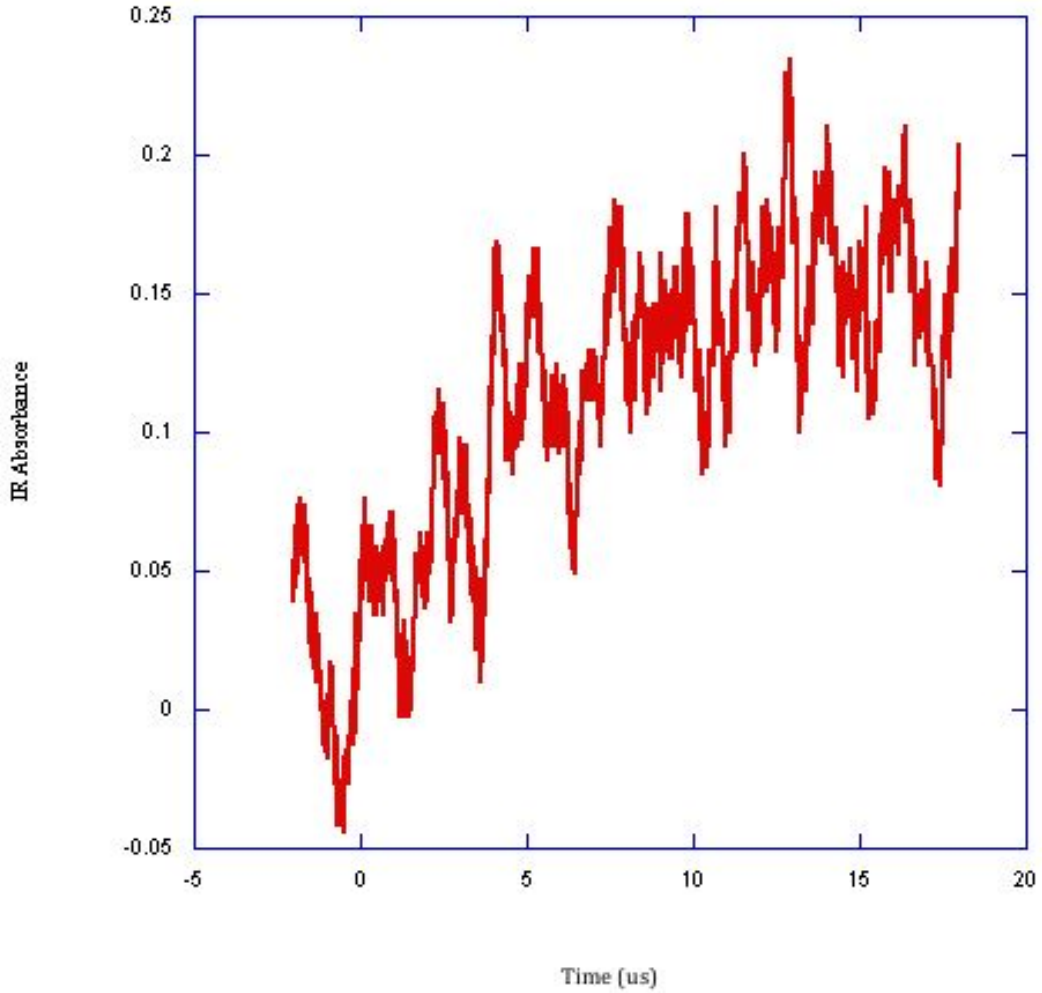

Figure 4.12 Transient from the center of the P36 pass shown in Figure 4.3. There is an overall trend towards higher absorbance but the noise obscures useful analysis. Compare this transient with the transient from P55 in Figure 3.1

of microseconds. Each electronic piece of instrumentation was carefully evaluated as a potential noise source. With only the IR diode and the detector powered, on the noise persisted. When every other instrument had been eliminated as a source of the noise, I concluded that the source of the noise must be the IR diode itself.

IR diodes do have slight fluctuations in frequency over very short time scales, called laser jitter. If the root cause of the noise is jitter then we should observe a variation in the magnitude of the noise depending on the spectral features. The magnitude of the noise should have a profile similar to the absolute value of the first derivative of the spectral features. Figure 4.13 helps illustrate how frequency jitter would cause noise in the transient signal. If the absorbance spectrum is close to constant at the base of a peak (a), meaning the derivative is close to zero, jitter to either side of the center frequency will measure similar absorbance values so the noise will be small. If the absorbance spectrum is strongly sloped on the side of a peak (b), meaning the derivative a large non-zero value, jitter to either side of the center frequency will measure vastly different absorbance values so the noise will be large. At the peak of the absorbance spectrum(c), the noise should decrease compared to the side as the change in absorbance is smaller over the range of the jitter.

To test this hypothesis, I performed a line width experiment on P41 with the UV laser blocked. Since there are no large energy transfer events without exciting the pyrazine, the transients were flat except for the noise. Then I fit these flat transients to a line and averaged the absolute value of the residuals, calling the quantity the noise level.

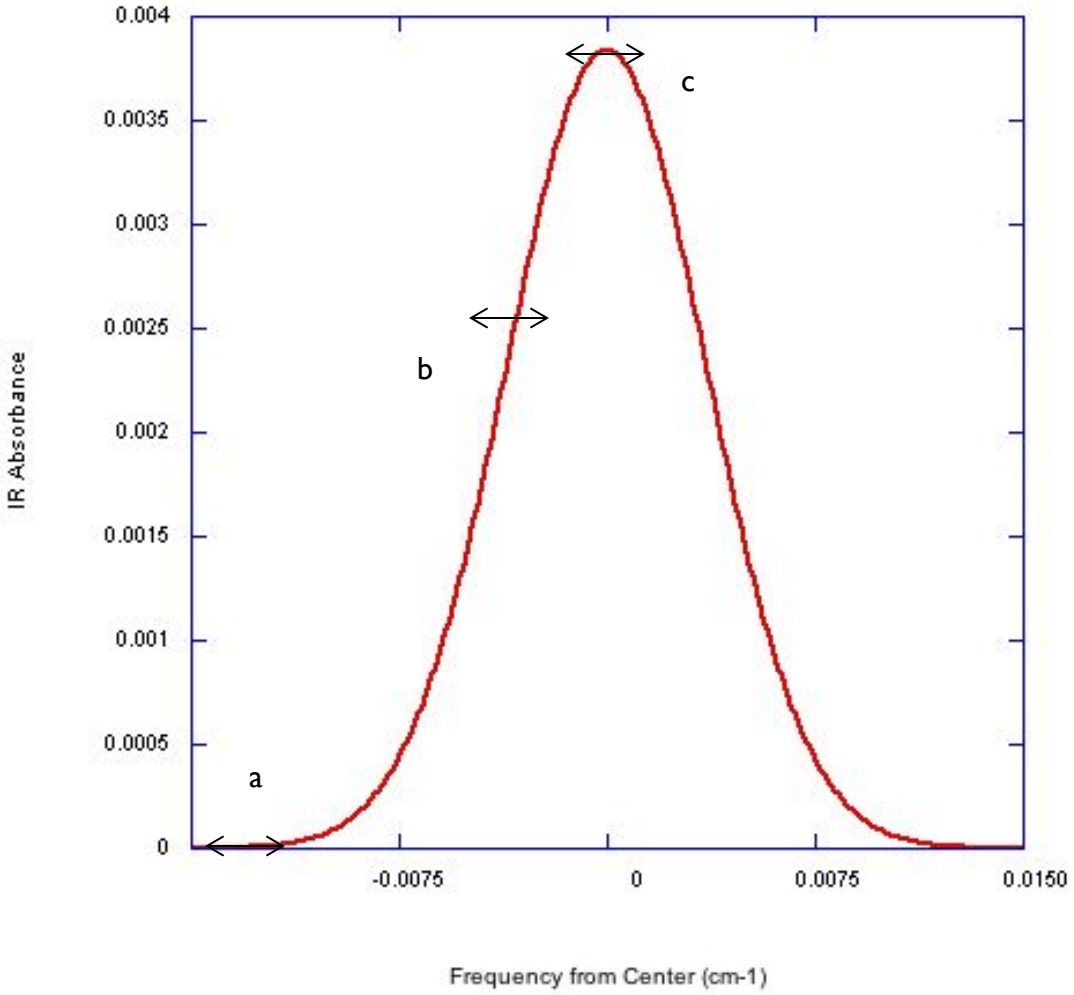

Figure 4.13 If the noise was caused by frequency jitter it would vary in magnitude depending on the absorbance spectrum. If the spectrum is flat (a) any frequency jitter will sample the same absorbance value and cause little noise. If the spectrum is steeply sloped on the shoulder of a peak (b), frequency jitter will sample very different frequencies and cause large noise fluctuations. At the center of a peak (c) the noise should decrease slightly as the differences in absorbance values have lessened.

The noise level for each transient along the line scan is plotted in Figure 4.14. It shows that on the edges of the P41 absorbance peak where the spectrum is flat there is little noise. And as the scan approaches the peak the noise increases. Most importantly there is a slight decrease in the noise level at the center, where the absorbance spectrum is peaked. This shows that the noise level does mimic the magnitude of the first derivative of the absorbance spectrum. Frequency jitter in the IR diode is the source of the noise in the low J state transients and line widths.

Transient absorption experiments are impossible to perform without the IR diode so we must reduce the effect of frequency jitter. Jitter will always be present in every diode to some degree and can be decreased by proper alignment, eliminating light feedback, and by curtailing mode hopping. Proper IR diode alignment is addressed in section IV, light feedback is addressed in section V and mode hopping in section VI. Overhauling the alignment and diode settings did not reduce the laser jitter sufficiently to provide useful low J state line widths. Since jitter is a systematic noise source it must be compensated for in any future work in the Sevy lab.

XII. Future Steps

I was unable to verify a solution for the noise caused by the laser jitter during my research due to external time constraints. An important question for future experiments is that if the noise is being caused by the laser jitter why it was not detrimental towards measuring the higher and mid J states. Comparing the transients from P36, Figure 4.10, and P55, Figure 3.1, the laser jitter noise is present for high J states at long times. At short times the noise has been overpowered by the increase in absorbance from molecules scattering into P55. Note the difference in scale of the P55 transient with the P36 transient. The P55

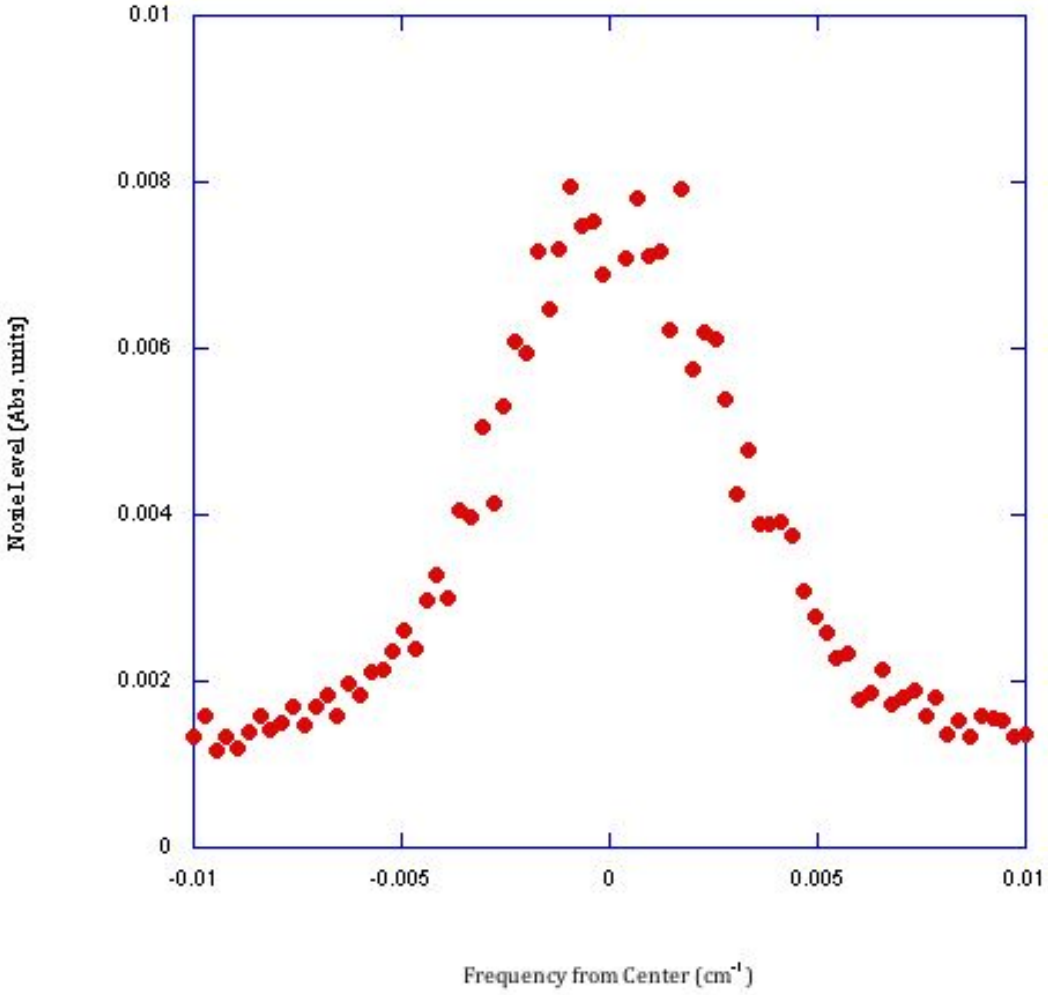

Figure 4.14 Noise level for P41. Noise level is calculated by fitting line width transients measured with the excimer laser blocked to a linear function and then averaging the residuals. This confirms that laser jitter is the major source of noise in the experiment for low J states. The noise level is low where the spectrum is less sloped and the jitter would sample regions of similar absorbance. Noise level increases where the spectrum is highly sloped and jitter would sample regions of differing absorbance. This confirms that laser jitter is the major source of noise in the experiment for low J states.

absorbance is an order of magnitude smaller. The reason laser jitter does not affect the higher J states is because they have much smaller absorbance signals due to their lower initial population. A Gaussian peak with smaller amplitude will have a smaller first derivative and thus less laser jitter noise, see section XI. To improve the low J state transients and decrease the noise, the overall absorbance must be decreased.

There are many different ways to decrease the absorbance in our experimental setup, some more applicable than others. If we were to decrease the pressure of the gases, the mean collision time would change and thus the rate of the energy transfer. Decreasing the pressure would also complicate comparisons to our previous studies Increasing the temperature would shift the population distribution to higher J states, decreasing the population in the lower J states and the absorbance. A meaningful shift in the population would require temperatures on the order of 1000 K, too high for boro-silicate glass sample chambers. The best solution is to decrease the length of the sample cell, which decreases the path length and the absorbance. Decreasing the path length has a minimal impact on the rest of the experiment as the alignment and collision time are not altered. It is also simple to implement. I am assuming that by decreasing the amplitude of the transient signal the slope and thus the line widths, see section X, are not affected. I am confident that shortening the sample cell to 5-10 cm will result in a decrease in the laser jitter noise. With a shorter cell, future members of the Sevy group will be able to measure the line widths of the low J states and improve upon the mid J state work. Combined with line center absorbances energy transfer rate constants and P(E´,E) can be calculated for the pyrazine-N_2O system.